# POLITECNICO DI TORINO

Department of Mechanical and Aerospace Engineering (DIMEAS)
Master's thesis in AUTOMOTIVE ENGINEERING

# Numerical design and experimental validation of a crash box with internal lattice structures

Supervisor:
**Prof. Andrea Tridello**

Co-supervisor:
**Prof. Davide Salvatore Paolino**
**Prof. Raffaele Ciardiello**
**Prof. Carlo Boursier Niutta**

Candidate:
**Alessandro De Masi**

*“When everything seems to be going against you,*

*remember that the airplane takes off against the wind,*

*not with it”*

*Henry Ford*

# Acknowledgements

I would like to thank my thesis supervisors Prof. Tridello Andrea, Prof. Paolino Davide Salvatore, Prof. Ciardiello Raffaele and Prof. Boursier Niutta Carlo for supporting me in this thesis work and for all the knowledge shared to me in this experience.

Last but not least, I appreciate the support of my family and my friends, always around me and helping me to reach this achievement.

Thank you very much sincerely to all of you.

# Abstract

The main aim of this thesis is to provide an experimental analysis of lattice structures for energy absorption and use them to correctly design a crash box produced by additive manufacturing technology. In particular, the development of a double full factorial plan led to the definition of the main factors of influence for this application. The initial lattice structure used to develop the full factorial plans has a morphology already studied in a previous thesis, in which the main goal was to select the most appropriate lattice morphology for energy absorption application. The material used for this study is a Carbon Nylon produced by FFF (Fused Filament Fabrication) technology that exploits interesting characteristics for this application and for lightweight design. The assessment of the properties of the different structures, taken into consideration in the factorial plans, is made through compression tests useful to evaluate energy absorption capacity (EA), specific energy absorption (SEA) and force versus displacement characteristics. Therefore, with this experimental approach it is possible to define different versions of the AM crash box and compare their performances with the performances of the Toyota Yaris crash box, to have an appropriate comparison with a real structure for automotive application.

# CONTENTS

# LIST OF FIGURES

# LIST OF TABLES

# CHAPTER 1

# Introduction

## 1.1 Additive manufacturing

Additive manufacturing (AM), or 3D printing, is a production technique that uses the deposition of materials to build of a three-dimensional object. The production process is based on the creation of a CAD (Computer Aided Design) model of the object (or component) that is used by a 3D printing system to produce the objects. The CAD model must be exported in a specific standard to be used by the printing process. One of the commonest format used by these systems STL (Standard Triangulation Language). STL basically converts the 3D model into a shell, in which the outer surface is discretized by triangles that vary their dimensions as a function of the requested resolution. This production technique is mainly adopted for rapid prototyping of tools, components or jigs. Many additive manufacturing machines need supports to build particular geometries that do not lean directly on the building plate to avoid shape distortion. These supports are usually included by the software of the 3D printing system as a function of the designed geometry and the specific characteristic of the production process. They are made of the same material of the part, or with a different material (dissolvable material) that can be easily removed. Finally, the geometry of the component is layered through the intersection with XY planes defined by a $\Delta Z$ offset, this phase is called slicing and it is used to fabricate the final object.

Once the fabrication process is completed, the object is removed from the plate and post-process operation are carried out. The post-process operations are related to support removal, post-curing, heat treatment (to restore residual tensions inside the structure due to the production process) and surface finishing (to improve the roughness for aesthetical or functional reasons). Additive manufacturing is a reliable and robust production process only under well controlled standardized conditions.

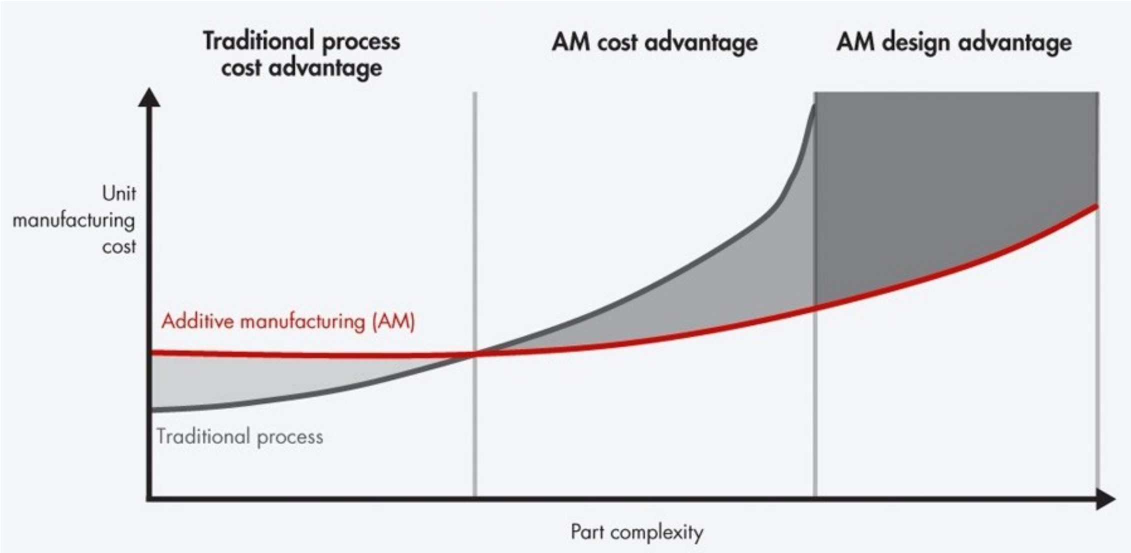


**FIGURE 1.1 - COST ADVANTAGE OF ADDITIVE MANUFACTURING**
(Source: *CAR – Center for Automotive Research [March 2019]*)

Although, the traditional manufacturing technologies such as casting, forging, injection moulding and machining present reduced costs for high volume production, AM presents reduced costs when the part complexity increases. This is shown in Figure 1.1, additive manufacturing costs do not increase significantly with parts that present a moderate complexity.

Other advantages of AM processes are focused on lightweight design, customization, freeform complexity, because this technique allow to shape objects that are not producible with standard machining process, increasing design freedom for designers. Obviously, there are also some disadvantages, that are limiting its use such as the costs related to low volume production, high production time and the limited size of the components that are determined by the size of the printing chamber.

The applications of additive manufacturing are several:

- Aerospace & Defence (crash boxes, jet engine fuel nozzle)
- Medical and Dental (prostheses, dental crowns, anatomic models, foot plates, screws for surgery)
- Automotive (motorsport's components, knuckle, intake manifold, exhaust pipe)
- Jewellery (customized rings)
- Lattice structures
- Living hinges and assemblies.

In this work, all the structure will be produced with a 3D printer Ultimaker 2+ Connect with the following specification (Figure 1.2):


| | |
|---|---|
| Build volume | 223 x 220 x 205 mm (8.7 x 8.6 x 8 inches) |
| Assembled dimensions | 342 x 460 x 580 mm (13.5 x 18.1 x 22.8 in) |
| Print technology | Fused filament fabrication (FFF) |
| Compatible filament diameter | 2.85 mm |
| Weight | 10.3 kg (22.7 lbs) |
| Power input | 100 - 240 VAC, 50 - 60 Hz |
| Maximum power output | 221 W |

**FIGURE 1.2 – ULTIMAKER2+ CONNECT**
(Source: *Ultimaker)*

The 3D printed material used for the production of experimental specimens and for the design of the crash box is a nylon-carbon filament. All the specimens are produced with the same process parameters, that are summarized here below in Figure 1.3.

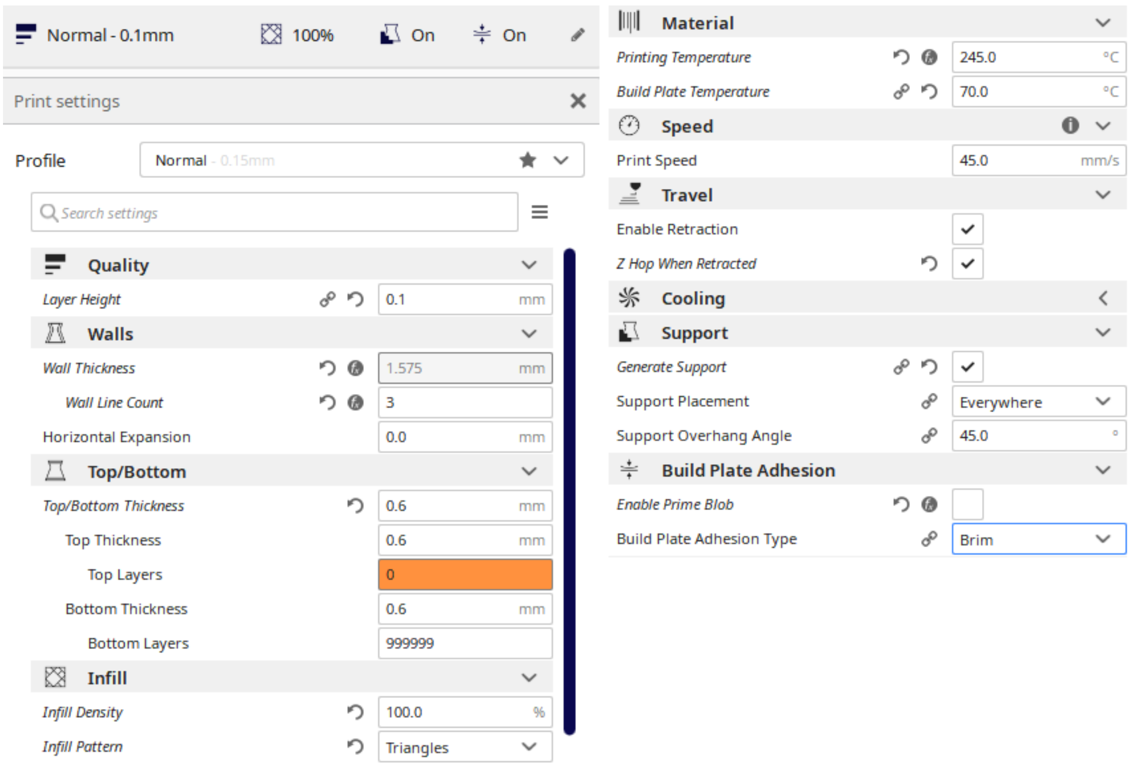


**FIGURE 1.3 - 3D PRINTING PROCESS PARAMETERS USED**

The mechanical properties used in the FEM models, in the following, are taken from the scientific paper *"Investigation of the Mechanical Properties of a Carbon Fibre-Reinforced Nylon Filament for 3D Printing"*[1].

[1] *Scientific paper: "Investigation of the Mechanical Properties of a Carbon Fibre-Reinforced Nylon Filament for 3D Printing" – Machines [September 2020]*

## 1.2 Literature review about crash boxes

Nowadays, the major trends concerning crashworthiness in automotive industry are related to the research of the optimal interface and layout between the vehicle and the passengers to provide maximum safety. In particular, passive safety components have to increase its overall crushing efficiency, i.e. having at least the same absorption capacity and a lower mass. Indeed, to meet an increasingly green vision, in favour of the protection of the environment and human health, the main request is related to the reduction of consumption and harmful emissions of passenger vehicles. These aspects are directly correlated to the mass of the vehicles, so, for those reasons composite materials, new manufacturing technologies and innovative solutions are increasing their use in this field exponentially.

The general configuration of a body in white automotive vehicle includes usually at least two or three load paths used to withstand the main loads that act on a car body in crash situations. The aim of the front frame assembly together with the compartment frames that are the body side and floor, is to manage the absorption of energy during a frontal crash and reduce potential injuries of fatalities of the occupants during the impact events. The main component designed in a suitable way to accomplish this task is a cantilever beam called longitudinal rail (PP) that should be joined directly to a resilient region of the compartment frame of the body. Many archetypes of the front assembly could be found as a function of the way the longitudinal member is linked to the remaining part of the body. Then, the front structure can include an upper rail (PS), an ancillary subframe (TI) and a front cross beam (TA). Another typical solution adopted is the introduction of crash boxes (CB), they are small boxed members placed usually between the front rail and bumper cross beam.

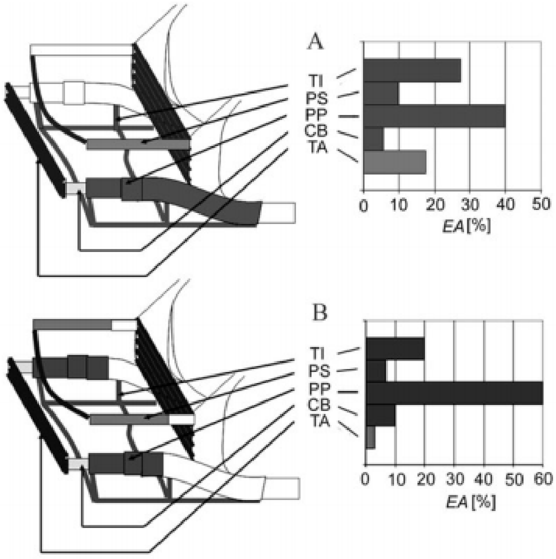


**FIGURE 1.4 - FRONT FRAME LAYOUT AND ENERGY ABSORPTION**
(Source: *Automotive Body – Volume I [2011]*)

In Figure 1.4, it is represented the most widespread layout configuration for the front frame of a body in white. As could be underlined, the contribution of the crash box during frontal crash at 56 km/h (A: offset rigid barrier – B: full overlap rigid barrier) is lower than 10% with respect to the overall energy absorption capacity. Crash boxes typically are structures mechanically fastened between the front bumpers and the longitudinal rails. They are used to absorb low-speed impacts in the range 10-15 km/h. Further, they should be able to collapse in the range of 10-15 km/h without introducing deformations in the rails, reducing significantly the repairing cost of the vehicle. Usually, crash boxes are pre-assembled components together with the bumper beam and carmakers assign to a single supplier the design of all the system subjected to low-speed impact.

Crash boxes have been widely studied during the years by research centres and automotive industry. This is still an active are of research and different crash boxes have been found and proposed in the literature to optimize the energy absorption during vehicle collision, the most widespread solutions are:

- **Extruded aluminium crash box**: Figure 1.5 shows an extruded aluminium crash box type that is a thin-walled structure very simple to be produced. However, they have a disadvantage related to the introduction of triggers that have to be applied with a post-manufacturing process.

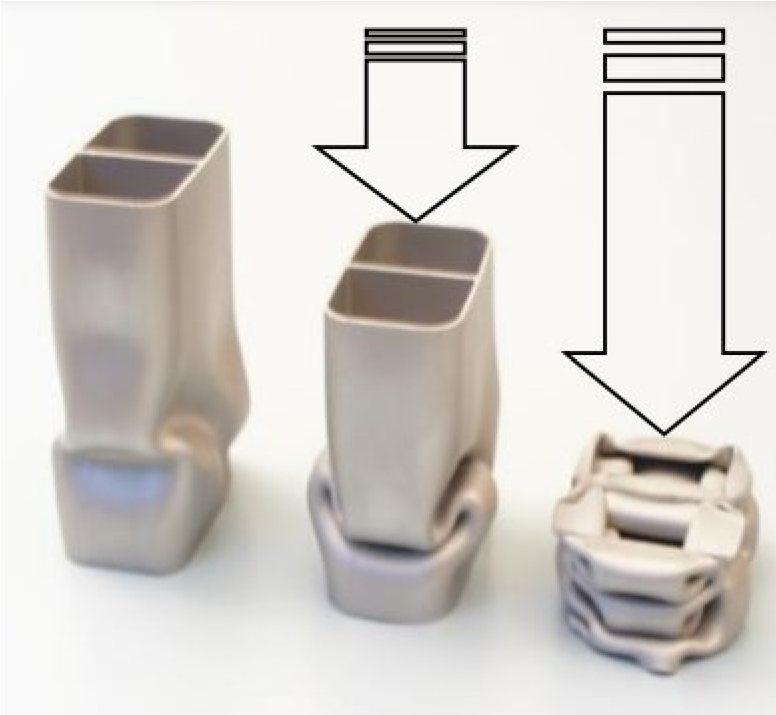

**FIGURE 1.5 - ALUMINIUM EXTRUDED CRASH BOX**
(Source: *Constellium*)

- **Welded steel crash box**: Figure 1.6 represents a welded solution that is a thin-walled structure produced usually by the joining of at least three steel shells (upper, lower and a plate) through welding. This solution allows to design complex geometries that include also triggers or a conic shape.

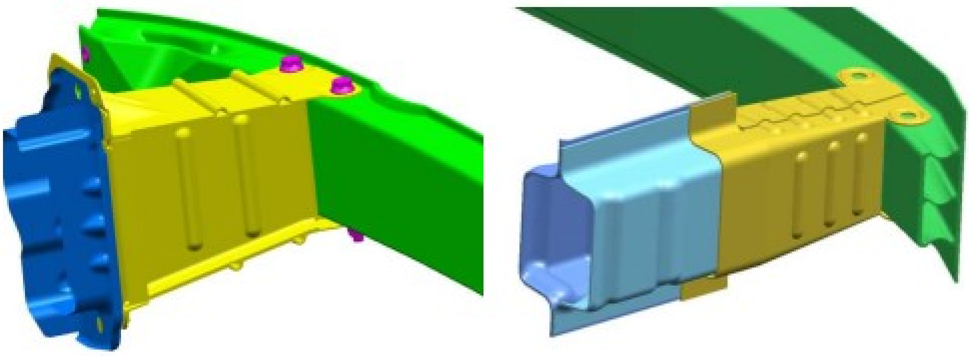

**FIGURE 1.6 - STEEL CRASH BOX**
(Source: *Constellium*)

- **Foam-filled crash box:** thin-walled structure in which a foam is introduced inside to improve the absorption capacity of the component, without increasing too much the mass.
- **Composite crash box:** thin-walled structure made in composite materials (i.e. CFRP or GFRP) to design a lightweight part using the high specific strength of these materials. This solution allows to shape very complex geometries that could be of monolithic or sandwich type, useful to reach high value and efficiency about energy absorption.

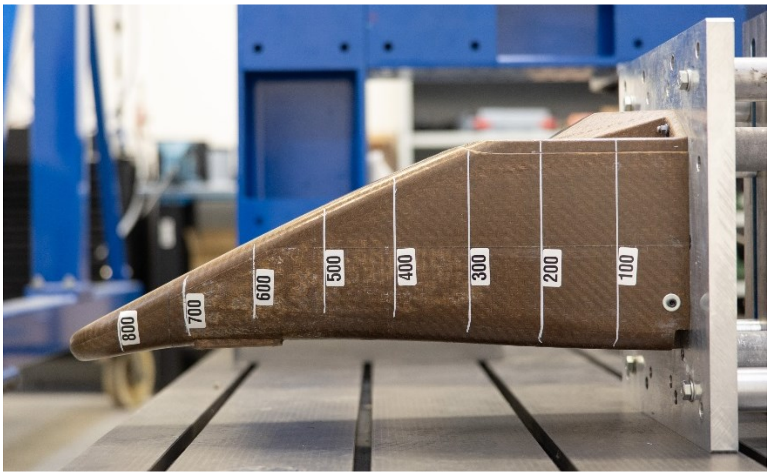


**FIGURE 1.7 - COMPOSITE CRASH BOX (NATURAL FIBER FIAS)**
(Source: *Composite World*)

Furthermore, it is possible to find solutions with different cross sections such as square, rectangular, circular, hexagonal that obviously lead to different performances and collapsing modes.

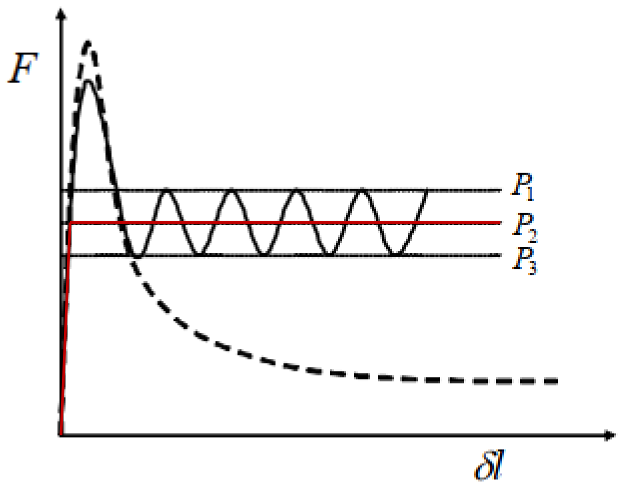


**FIGURE 1.8 - FOLDING (SOLID LINE), GLOBAL INSTABILITY (DASHED LINE) AND IDEAL CRUSHING BEHAVIOUR (RED LINE)**
(Source: Morello, Rossini, Pia and Tonoli [2011])

One of the most important factors for crash boxes that must be taken into account is the crushing behaviour. The folding and global instability deformation mechanisms with respect to the ideal one (red line) are compared in Figure 1.8. The dashed line shows the mechanical response of the structure when compression instability occurs at global level. This collapsing mode led to a drop of efficiency. Clearly, the folding mode is the most convenient for the energy absorption, as it leads to plastic deformation a large portion of the structure with respect to the global instability in which the plastic deformation is limited only to the so-called knee and to the ends. It is possible to induce the folding mode, in thin-walled structures, overcoming the global instability, with the local instabilities by introducing triggers in specific regions of the component. Considering thin-walled structure with rectangular cross section, critical stress of compression can be computed as follow:

$$\sigma_{cr} = k\frac{\pi^2 E}{12(1-\nu^2)}\left(\frac{t}{b}\right)^2 \tag{1.1}$$

where k is a parameter functions of the side dimension of the cross section, and of the ratio $\lambda = l/m$ between the number m of half-waves that can be formed after the instability along the loading direction (side *l*). Figure 1.9, represented below, underlines all the geometrical dimensions of interest.

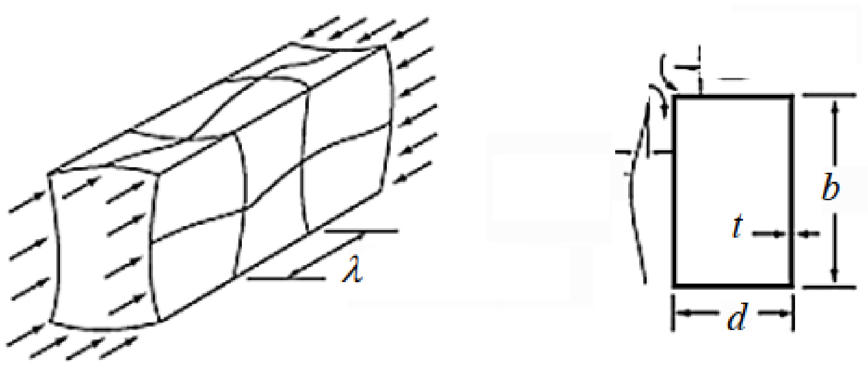


**FIGURE 1.9 - ELASTIC INSTABILITY OF A THIN-WALLED BEAM (RECTANGULAR CROSS SECTION)**

(Source: Prof. Tonoli – Passive Safety Notes)

As already stated, global instability can be triggered by the local ones if the ratio *t/b* is small enough to induce instability in the elastic range, i.e. $\sigma_{cr} < \sigma_y$. In the case in which the critical stress overcome the elastic field, the equation (1.1) must be modified in order to take into account plastic deformation:

$$\sigma_{cr} = \frac{\pi^2 E_s}{9}\left(\frac{t}{b}\right)^2\left\{\left(\frac{1}{4}+\frac{3}{4}\frac{E_t}{E_s}\right)\left(\frac{mb}{l}\right)^2 + 2 + \left(\frac{l}{mb}\right)\right\} \tag{1.2}$$

where $E_s$ and $E_t$, respectively the secant and tangent moduli, replace the elastic modulus in the equation.

So, as general rule, global instability of the crash boxes must be avoided and the efficiency of the crushing behaviour of the structures could be improved increasing the proportion of material that lead to plastic deformation. For all abovementioned reasons, additive manufacturing technology can lead to several advantages because of the possibility to increase the geometry complexity due to the absence of manufacturing constraints.

## 1.3 Methodology

The effective workflow adopted for this work is based on three different stages:

- Design of the suitable geometry (CAD)
- Finite Element Analysis (FEA)
- Experimental evaluation

Such procedure is fundamental to evaluate in a correct way the mechanical characteristic of a component. Indeed, for additive manufacturing structure, the mechanical characteristics of the components are very sensitive to the building process, the proposed workflow is powerful to predict through simulation the real behaviour of lattice structures. For this purpose, different software has been used. PTC Creo Parametric is used for the creation of the concepts and geometries in which is included a specific tool for the creation of lattice structures also allowing a characterization of key geometrical parameters such as cross section area of the lattice, volume and mass. The development of the FEA models, instead, have been performed in three different levels:

1. Discretization is performed through Altair Hypermesh;
2. BCs and properties assessment through LS-Dyna;
3. Results evaluation and plotting though Altair Hypergraph and Excel.

The structures are discretized via 1D type beam elements in order to reduce the memory and running time requirements for the analysis. Obviously, the use of 3D elements certainly leads to more accurate results including geometrical factors like radius and fillets between the beams of the structure or also physical factors such as local stress concentration or mechanical instabilities, fracture criterion.

The 1D element formulation used in LS – Dyna is the Hughes-Liu with cross section integration. It exploits the following capabilities:

- It is incrementally objective (rigid body rotation don’t induce strains);
- It is efficient and robust;
- It includes the evaluation of transverse shear strains.

The Hughes-Liu beam element formulation is based on the transformation of the isoparametric 8-node solid element into a 1D representation. Starting from the, so called, Biunit Cube definition is possible to transform them into a local coordinate system representative of the beam element as represented graphically in Figure 1.10.

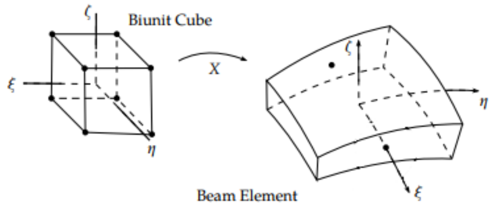


**FIGURE 1.10 – DEGENERATION OF ISOPARAMETRIC 8-NODE FORMULATION**
(Source: LSTC – LS-DYNA Theory Manual)

The effective definition of the element requires the following parameter:

- A: cross section area;
- CST: Cross section type useful to define the inertia tensor of the beam;
- QR: Quadrature rule to define the integration point on the section area.

The definition of the mechanical characteristic of the material used is requested after the correct definition of the geometrical properties of the lattice. The MAT24 (PIECEWISE LINEAR PLASTICITY) is chosen as material formulation with the aim to include the plastic behaviour of the Carbon Nylon. So, the mechanical constant has been evaluated starting from the tensile test curve showed in the scientific paper [1].

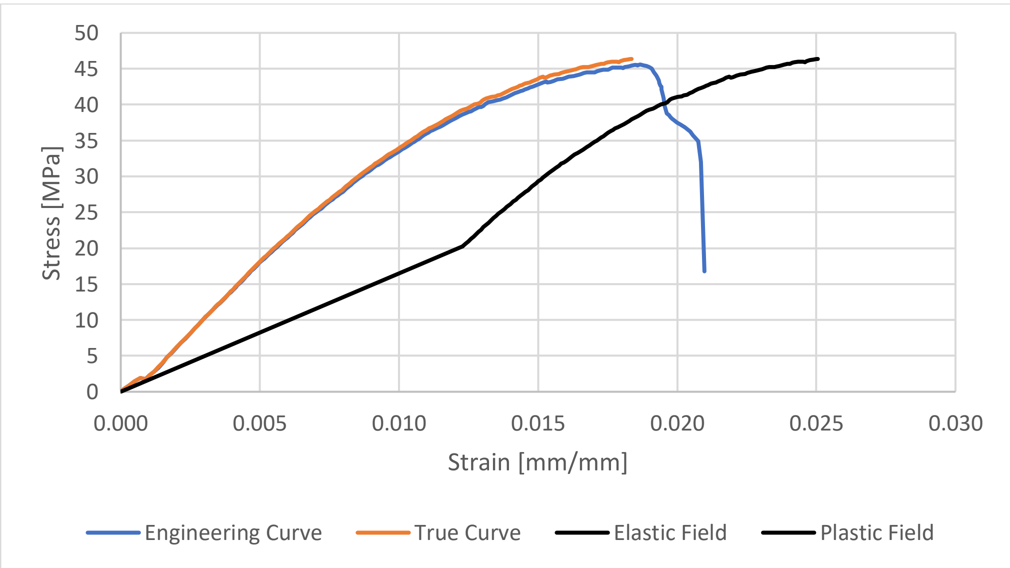


**FIGURE 1.11 - CARBON FIBRE-REINFORCED NYLON TENSILE CURVE**

Starting from the tensile test curve, performing a linear regression (Figure 1.12) it is possible to evaluate the Young Modulus.

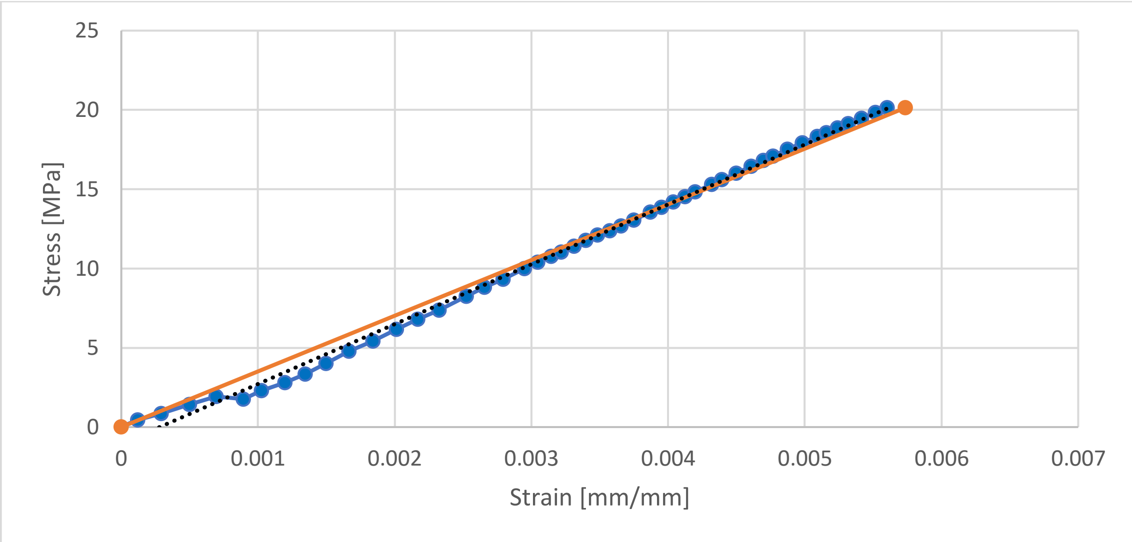


**FIGURE 1.12 - LINEAR REGRESSION FOR YOUNG MODULUS ESTIMATION**

The engineering curve is converted into the true one and isolate the plastic field for a correct definition of MAT24. The resulting curve is shown in Figure 1.13 and the useful mathematical relations for the conversion are reported below in Equation 1.3 and 1.4:

$$\begin{cases} \varepsilon = \ln(1+e) \\ \sigma = \sigma_{eng}(1+e) \end{cases} \tag{1.3}$$

$$\varepsilon_{plast} = \varepsilon_{true}{}^{tot} + \sigma_{y,true}\left(\frac{1}{E_{ref}} - \frac{1}{E_{regr}}\right) \tag{1.4}$$

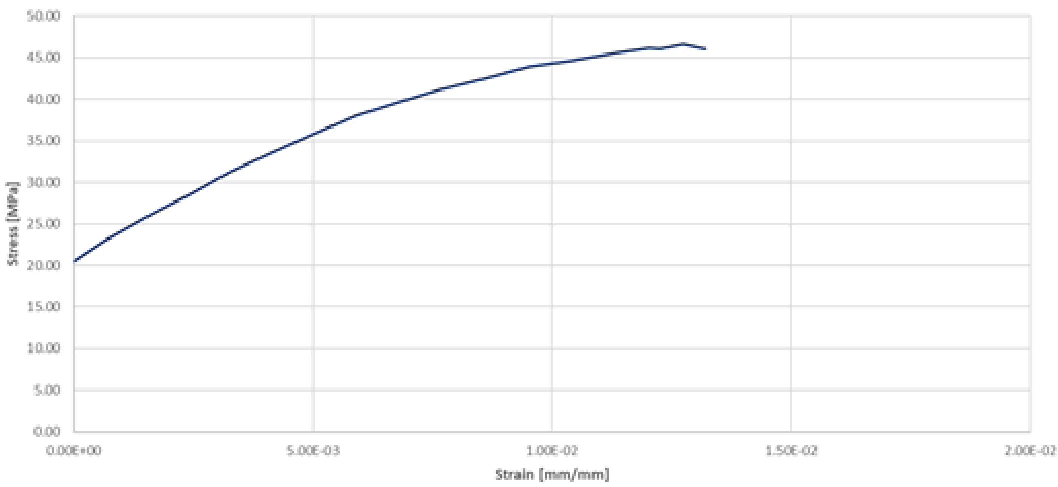


**FIGURE 1.13 - TRUE PLASTIC CURVE CARBON NYLON**

Analysing the curve of Figure 1.11, it is possible to notice a small shift at the beginning of the test due to a little slide between the specimen and the holder. For this reason, the linear regression is performed in such a way to determine the modulus passing through the origin of the axis, neglecting the issue. Obviously, the resulting $R^2$ parameter equal to 0.98 determine the modulus evaluated with this procedure it could be considered representable of the set of data.

At this point, all the parameter needed to correctly set MAT 24 have been evaluated and reported here in Table 1.1.

**Carbon Fibre-Reinforced Nylon (3D Printed)**

| E [MPa] | $\sigma_y$ [MPa] | $\sigma_{UTS}$ [MPa] | $\rho$ [g/cm$^3$] | $\nu$ [-] |
|---|---|---|---|---|
| 3510.62 | 20.25 | 45.96 | 1.14 | 0.35 |

**TABLE 1.1 – CARBON NYLON MATERIAL PARAMETER**

# CHAPTER 2

# Full factorial design

One of the main aim of this work it to provide a procedure for the design of crash boxes made of lattice structures. For this reason, Design of Experiments (DoE) has been adopted to experimentally assess the parameters that mostly affect absorption capacity of lattice structures. Therefore, basing on a previous thesis that has established the best lattice structure geometry and cell for crash application, the characteristics of the lattice structures have been analysed focusing on two aspects:

- Establishing which are the factors of influence, in terms of diameter of the beams and number of cells, fixing the total volume equal to the one of the lattice structure evaluated in a previous thesis, to determine the best configuration.
- Understand which are the factors of influence of the repetition in space of the same lattice structure considering different beam's diameters and number of repetition.

Accordingly, two factorial plans are developed to analyse the two main aspects described above. In the following, they will be identified with the acronymous FFP1 and FFP2 correspondingly.

Parameters like $F_{max}$ (PCF), $F_{avg}$ (MCF) have been described in detail in the Introduction Section. Other important parameters taken into consideration in the following are CFE (Crush Force Efficiency), SEA (Specific Energy Absorption), $\Delta F$.

The parameter CFE is a measure of the efficiency of the structure, i.e. it takes into consideration the difference between the peak force and the mean force after the peak. In this way, the difference between the mechanical characteristics of the structure during the compression and the ideal behaviour can be quantified. For example, it can be useful to assess the drop in performance if the structure reaches the global instability, i.e. it shows a very large difference between the PCF and MCF.

The SEA is the key parameter for comparing absorption capability with respect to the mass of the component. It must be noted that the calculation of SEA is performed in a range in which the mechanical characteristic of the structure shows a quite constant MCF, as represented in Figure 2.1.

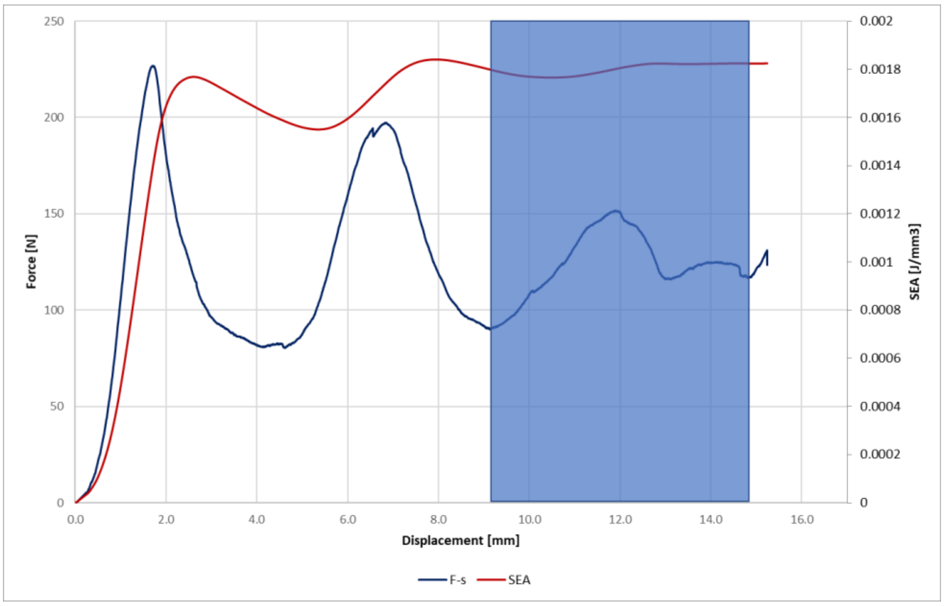


**FIGURE 2.1 - EXAMPLE OF SEA CALCULATION**

The factorial design is based on two factors, i.e. the beam diameter (Factor A) and the number of cells given the specimen volume (Factor B). Moreover, four levels have been considered for Factor A, three levels for Factor B. The factors and levels are defined taking into consideration physical and practical constraints due to 3D printing manufacturing process. For example, the minimum physical diameter of a beam that can be produced is 0.9 mm and, for FFP1, the maximum cell number repetition per unit volume of 19.68 $cm^3$ corresponds to a 4x4 structure.

Table 2.1 summarized the factors and levels considered in this analysis.

| | LEVELS | | | |
|---|---|---|---|---|
| Factor A | 1 | 2 | 3 | 4 |
| Diameter Beams | 0,9 mm | 1,2 mm | 1,5 mm | 1,8 mm |

| | LEVELS | | |
|---|---|---|---|
| Factor B | 1 | 2 | 3 |
| Cell Number | 2 x 2 | 3 x 3 | 4 x 4 |

**TABLE 2.1 - LEVELS AND FACTORS OF FACTORIAL PLANS**

Starting from the definition the factors and levels it is decided to develop an orthogonal factorial plan, which results in the following arrangement (Table 2.2):

| FACTORS | | |
|---|---|---|
| # Test Identification Number | A | B |
| 1 | 1 | 1 |
| 2 | 1 | 2 |
| 3 | 1 | 3 |
| 4 | 2 | 1 |
| 5 | 2 | 2 |
| 6 | 2 | 3 |
| 7 | 3 | 1 |
| 8 | 3 | 2 |
| 9 | 3 | 3 |
| 10 | 4 | 1 |
| 11 | 4 | 2 |
| 12 | 4 | 3 |

**TABLE 2.2 - FACTORIAL PLAN DESIGN**

Therefore, the test identification number can be useful in order to establish an unequivocal identification code for each structure. The first numerical digits of the code represent the test identification number used to understand to which factor and level each structure correspond. Then, it is included the text "Cella_04" that represent the lattice structure designed in the thesis work *"Provini in struttura lattice realizzati mediante fabbricazione additiva: Simulazione di prove statiche e di impatto e validazione sperimentale"*[2] to identify the unit lattice structure considered. Then, the end of the code includes an identification text used to identify to which factorial plan it corresponds.

Generally speaking, SEA is computed according to Equation 2.1:

$$SEA = \frac{EA}{V} \tag{2.1}$$

The calculation of the compressed volume in the range of interest is considered as the product between the $A_{avg}$ and the displacement applied to the structure. The need to consider the average area is due to the variability of the area of the lattice as a function of

[2] *M.Sc. Thesis: "Provini in struttura lattice realizzati mediante fabbricazione additiva: Simulazione di prove statiche e di impatto e validazione sperimentale" – Mariano Della Ripa [2020-2021]*

the Z coordinate. Therefore, 85 - 100 different sections are defined in Creo with a step of 0.075 – 0.01 mm to evaluate the corresponding minimum and maximum area of each structure of the factorial plans, defining in this way the average area of the corresponding cell. Tables 2.3 and 2.4 show the resulting value of areas.

| Test | $A_{min}$ | $A_{max}$ | $A_{avg}$ |
|---|---|---|---|
| 01_Cella_04_FFP1 | 21.59 | 123.19 | 38.82 |
| 02_Cella_04_FFP1 | 46.95 | 180.16 | 81.90 |
| 03_Cella_04_FFP1 | 84.90 | 233.38 | 133.63 |
| 04_Cella_04_FFP1 | 38.06 | 161.47 | 66.35 |
| 05_Cella_04_FFP1 | 83.47 | 233.73 | 137.00 |
| 06_Cella_04_FFP1 | 150.47 | 299.92 | 220.07 |
| 07_Cella_04_FFP1 | 59.16 | 198.30 | 99.55 |
| 08_Cella_04_FFP1 | 130.422 | 284.062 | 200.475 |
| 09_Cella_04_FFP1 | 232.049 | 360.634 | 314.044 |
| 010_Cella_04_FFP1 | 84.908 | 233.670 | 137.442 |
| 011_Cella_04_FFP1 | 187.805 | 331.154 | 268.987 |
| 012_Cella_04_FFP1 | 335.957 | 460.427 | 407.709 |

TABLE 2.3 - AVERAGE AREAS OF FACTORIAL PLAN 1

| Test | $A_{min}$ | $A_{max}$ | $A_{avg}$ |
|---|---|---|---|
| 01_Cella_04_FFP2 | 27.41 | 84.37 | 42.83 |
| 02_Cella_04_FFP2 | 46.95 | 180.16 | 81.90 |
| 03_Cella_04_FFP2 | 96.55 | 328.18 | 157.90 |
| 04_Cella_04_FFP2 | 46.14 | 111.72 | 71.86 |
| 05_Cella_04_FFP2 | 83.47 | 233.73 | 137.00 |
| 06_Cella_04_FFP2 | 171.65 | 430.66 | 264.31 |
| 07_Cella_04_FFP2 | 51.94 | 138.67 | 105.54 |
| 08_Cella_04_FFP2 | 130.422 | 284.062 | 200.475 |
| 09_Cella_04_FFP2 | 200.805 | 528.133 | 386.942 |
| 010_Cella_04_FFP2 | 57.219 | 165.449 | 142.206 |
| 011_Cella_04_FFP2 | 187.805 | 331.154 | 268.987 |
| 012_Cella_04_FFP2 | 219.817 | 622.781 | 519.414 |

TABLE 2.4 - AVERAGE AREAS OF FACTORIAL PLAN 2

The experimental activity is based on compression tests used to evaluate and analyse the key factors in terms of energy absorption. All the tests are performed on a Zwick Z100 materials testing machine (Figure 2.2) with test speed of 1-2 mm/s.


**FIGURE 2.2 - ZWICK Z100 TESTING MACHINE**

In addition, a system of video acquisition is set to record the experimental tests, useful for post-processing of the results in terms of analysis of the collapsing mechanism of each structure. A sample of a recorder frame is here reported in Figure 2.3.

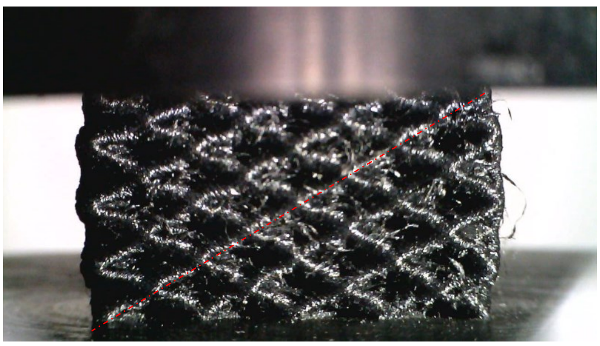

**FIGURE 2.3 - EXAMPLE OF A FRAME RECORDED WITH THE VIDEO ACQUISITION**

# 2.1 Full factorial plan 1 (FFP1)

The experimental plan FFP1 is developed to understand which are the factor of influence for a fixed volume of the tested specimen (reference volume in the following), corresponding to the one defined in a previous thesis [1]. The reference volume corresponds to a cube of 25.5 x 25.5 x 25.5 mm. Accordingly, the cell size has been varied by keeping the specimen volume, i.e. the number of cells for each specimen varied according to Table 2.1. The CAD files of the tested specimens have been developed with the use of the lattice design tool included in PTC Creo software.

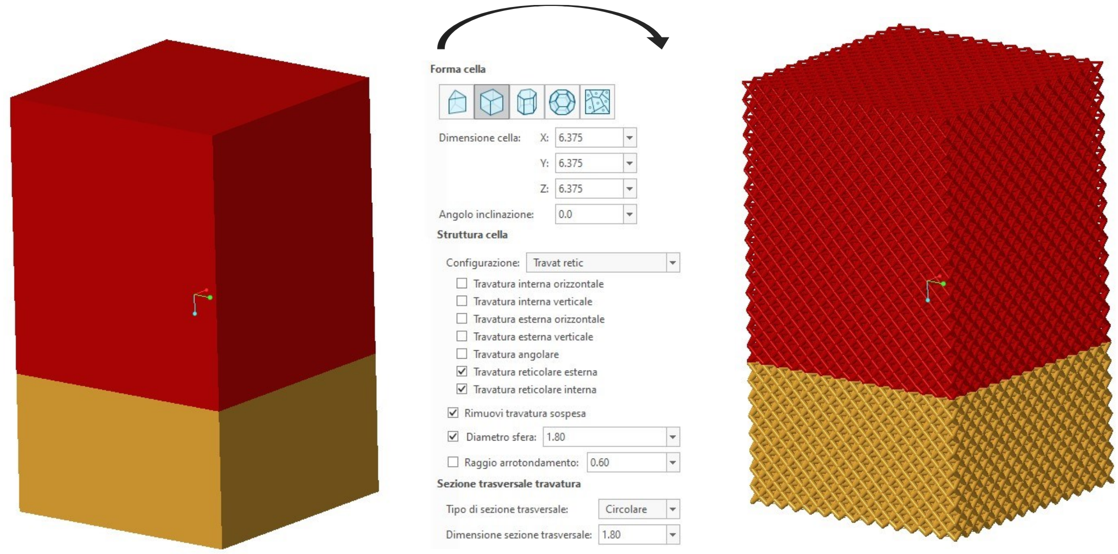


**FIGURE 2.4 - PTC CREO TOOL DESIGN FOR LATTICE STRUCTURE**

Figure 2.4 explains the design approach using this tool. The general shape of the component is defined as in standard CAD system, then through the use of the dedicated tool it is possible to define the morphology of the lattice structure. In our case, it is chosen to substitute completely the initial component with the desired lattice structure. There is also a dedicated section for the design variable lattice structure (Figure 2.5).

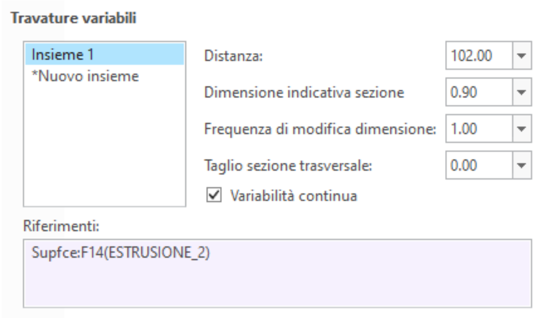


**FIGURE 2.5 - VARIABLE LATTICE STRUCTURE DEFINITION**

In the case represented above, starting from a diameter of the lattice beams equal to 1.8 mm, it is defined the variable region setting the distance along the vertical axis equal to 102 mm, the target diameter equal to 0.9 mm and the frequency factor equal to 1 in order to define a linear variation along the desired direction.

For each specimen type two tests are performed to verify the experimental scatter, a sample of the produced structures are here reported in Figure 2.6.

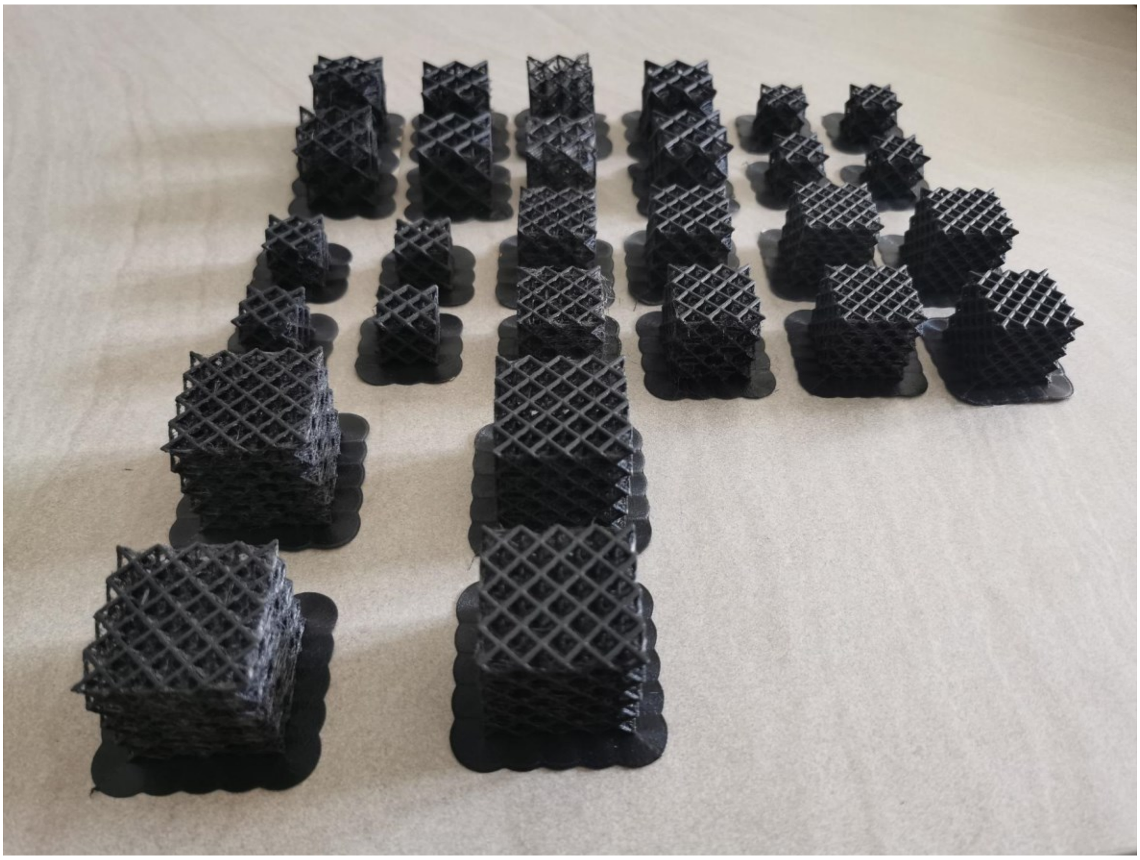

**FIGURE 2.6 - SAMPLE OF LATTICE SPECIMENS FOR EXPERIMENTAL TESTS**

The results of FFP1 are summarized in the Table 2.5:

| | EA | SEA MAX | SEAavg | δIN | δend | MCF | PCF | CFE | EA | SEA MAX | SEAavg | δIN | δend | MCF | PCF | CFE |
|---|---|---|---|---|---|---|---|---|---|---|---|---|---|---|---|---|
| | J | J/mm3 | J/mm3 | mm | mm | [N] | [N] | [N/N] | J | J/mm3 | J/mm3 | mm | mm | [N] | [N] | [N/N] |
| CELLA 01 | 0.41 | 0.00 | 0.00 | 10.20 | 13.70 | 28.45 | 41.34 | 0.69 | **0.42** | 0.0007 | **0.0006** | 10.13 | 13.60 | 29.14 | 38.54 | **76%** |
| | 0.44 | 0.00 | 0.00 | 10.05 | 13.50 | 29.84 | 35.75 | 0.83 | | | | | | | | |
| CELLA 02 | 2.77 | 0.00 | 0.00 | 5.92 | 13.17 | 249.74 | 361.96 | 0.69 | **2.58** | 0.0023 | **0.0022** | 6.51 | 13.54 | 221.02 | 304.84 | **73%** |
| | 2.39 | 0.00 | 0.00 | 7.10 | 13.90 | 192.30 | 247.73 | 0.78 | | | | | | | | |
| CELLA 03 | 5.91 | 0.00 | 0.00 | 6.60 | 11.94 | 535.24 | 596.40 | 0.90 | **5.74** | 0.0034 | **0.0031** | 6.66 | 12.29 | 541.34 | 607.70 | **89%** |
| | 5.58 | 0.00 | 0.00 | 6.72 | 12.65 | 547.43 | 619.00 | 0.88 | | | | | | | | |
| CELLA 04 | 2.07 | 0.00 | 0.00 | 8.33 | 13.46 | 138.90 | 239.68 | 70% | **1.93** | 0.0019 | **0.0019** | 8.67 | 14.16 | 131.53 | 233.24 | **62%** |
| | 1.79 | 0.00 | 0.00 | 9.00 | 14.86 | 124.15 | 226.79 | 0.55 | | | | | | | | |
| CELLA 05 | 6.42 | 0.00 | 0.00 | 7.00 | 10.33 | 587.77 | 827.80 | 0.71 | **5.18** | 0.0031 | **0.0029** | 7.55 | 10.57 | 483.16 | 691.45 | **70%** |
| | 3.95 | 0.00 | 0.00 | 8.11 | 10.80 | 378.56 | 555.09 | 0.68 | | | | | | | | |
| CELLA 06 | 18.94 | 0.01 | 0.01 | 8.51 | 12.11 | 1830.44 | 1990.54 | 0.92 | **18.94** | 0.0070 | **0.0065** | 8.15 | 12.05 | 1883.15 | 2044.94 | **92%** |
| | 18.95 | 0.01 | 0.01 | 7.80 | 12.00 | 1935.86 | 2099.34 | 0.92 | | | | | | | | |
| CELLA 07 | 5.42 | 0.00 | 0.00 | 10.01 | 13.61 | 368.00 | 645.22 | 0.57 | **5.27** | 0.0037 | **0.0033** | 8.21 | 13.36 | 382.95 | 653.37 | **59%** |
| | 5.12 | 0.00 | 0.00 | 6.41 | 13.11 | 397.90 | 661.52 | 0.60 | | | | | | | | |
| CELLA 08 | 22.57 | 0.01 | 0.01 | 12.20 | 15.38 | 1957.87 | 2441.13 | 0.80 | **35.56** | 0.0112 | **0.0104** | 12.15 | 15.69 | 3210.46 | 3702.52 | **85%** |
| | 48.55 | 0.02 | 0.01 | 12.10 | 16.00 | 4463.05 | 4963.90 | 0.90 | | | | | | | | |
| CELLA 09 | - | - | - | - | - | - | - | - | **41.83** | 0.0102 | **0.0089** | 10.00 | 13.00 | 6243.45 | 6540.51 | **95%** |
| | 41.83 | 0.01 | 0.01 | 10.00 | 13.00 | 6243.45 | 6540.51 | 0.95 | | | | | | | | |
| CELLA 10 | 7.45 | 0.00 | 0.00 | 5.70 | 12.90 | 634.83 | 1042.51 | 0.61 | **8.88** | 0.0049 | **0.0044** | 5.95 | 13.10 | 723.54 | 1137.99 | **63%** |
| | 10.31 | 0.01 | 0.01 | 6.20 | 13.30 | 812.26 | 1233.46 | 0.66 | | | | | | | | |
| CELLA 11 | 35.79 | 0.01 | 0.01 | 12.00 | 14.30 | 3956.77 | 4271.10 | 0.93 | **35.88** | 0.0093 | **0.0086** | 11.58 | 14.33 | 3973.06 | 4292.57 | **93%** |
| | 35.98 | 0.01 | 0.01 | 11.16 | 14.37 | 3989.34 | 4314.04 | 0.92 | | | | | | | | |
| CELLA 12 | 90.05 | 0.02 | 0.02 | 10.50 | 12.00 | 13552.76 | 14049.50 | 0.96 | **90.05** | 0.0184 | **0.0174** | 10.50 | 12.00 | 13552.76 | 14049.50 | **96%** |
| | - | - | - | - | - | - | - | - | | | | | | | | |

**TABLE 2.5 – TEST RESULTS OF FACTORIAL PLAN 1**

According to Table 2.5, the efficiency in terms of energy absorption increase with the relative density, i.e. the percentage of fulfilment of the volume at disposal. In fact, all the key parameters increase from 2x2 to 4x4 configuration and also by increasing the diameter of the internal beams. It could be interesting because increasing the relative density the lattice structure behaves as a foam substantially.

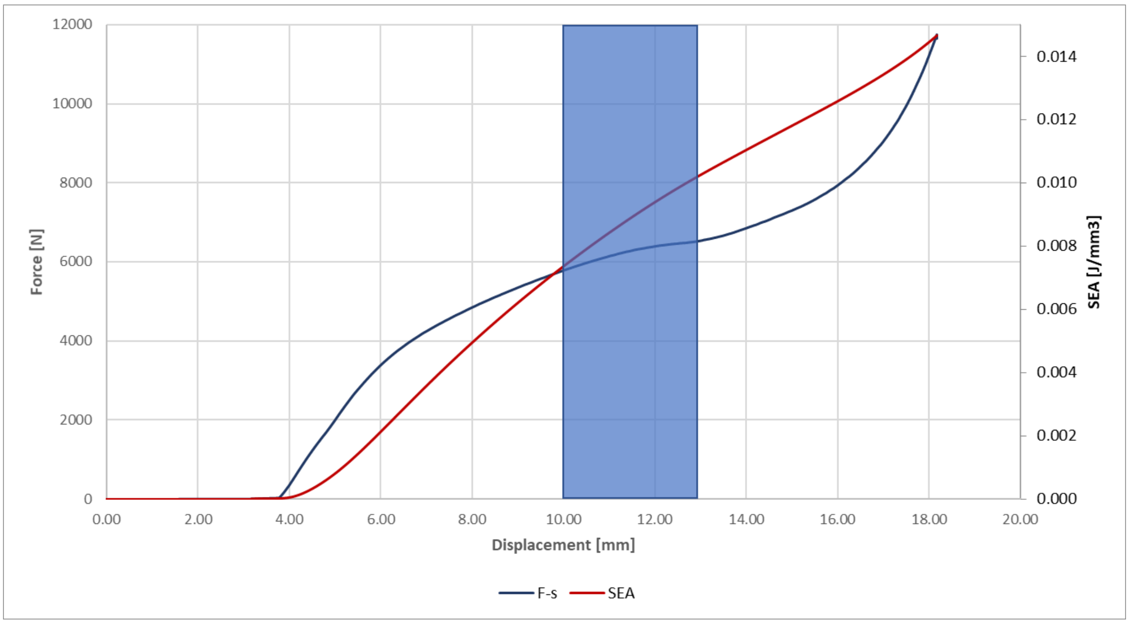


**FIGURE 2.7 - EXPERIMENTAL RESULTS OF 09_CELL_04_FFP1**

Taking as example the results of 09_Cell_04_FFP1 reported in Figure 2.7, it shows in a first phase a linear response up to a certain limit, after which reaching local instabilities of the internal beams the force remains almost constant exploiting a plateau. Then, when all the beams are deformed the structure shows a densification phase.

The critical load ($P_{cr}$), according to the general Euler Instability equation for a straight beam, is function of the Young Modulus of the material (E), the inertial moment (J) and the effective length (L) of the beam. The mathematical relation is here reported in Equation 2.2:

$$P_{cr} = \pi^2 E \frac{J}{L^2} \tag{2.2}$$

So, by increasing the diameter of the beam the critical load increases too, with a subsequent rise of the energy absorbed and SEA. In the same way, from a 2x2 to a 4x4 configuration with a fixed volume, the structure will exploit better characteristics concerning the absorption of energy because it means that the characteristic length L will be lower, determining a higher critical load.

For a better understanding of the data, an ANOVA (Analysis of Variance) was carried out to assess which factors are really influencing the structure's performance. The normality of the experimental data was at first verified. To verify if the data are normally distributed it can be useful to represent them into the so-called normality plot. It is reported for each factor in Figure 2.8.

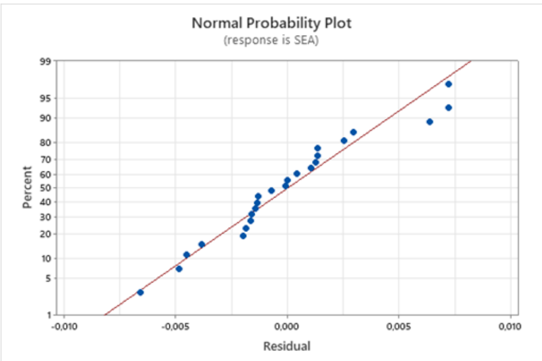


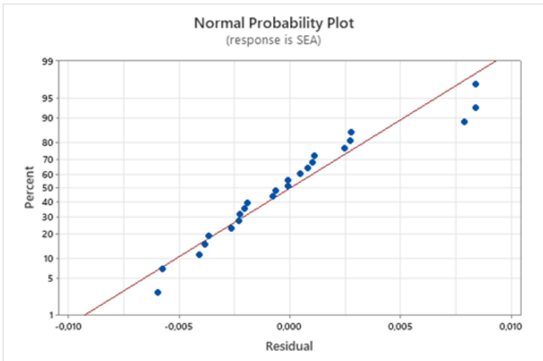


**FIGURE 2.8 – NORMALITY PLOT OF FFP1 DATA**

Every single factor is normally distributed, because the data are close to the straight line. However, considering all the factors as a whole, it is possible to plot again the normality plot and build the corresponding Gaussian curve starting from the histogram representation.

The result of this procedure is reported in Figure 2.9.

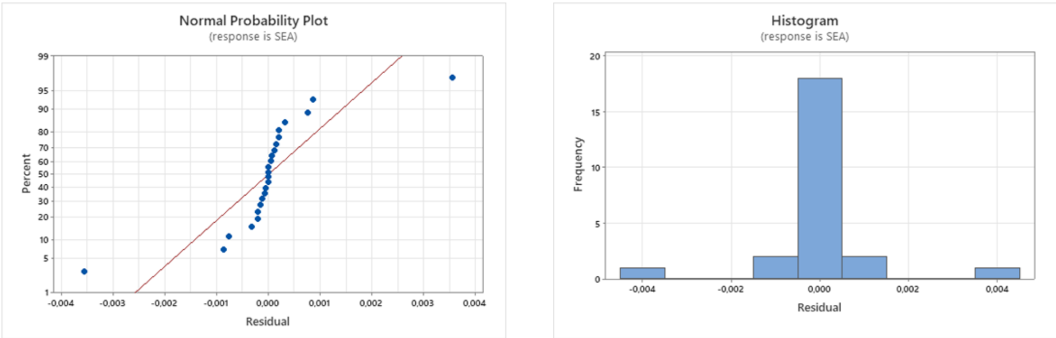


**FIGURE 2.9 – NORMALITY PLOT AND HISTOGRAM OF CUMULATED DATA OF FFP1**

Even if the normality plot of the cumulated factors shows again a well-fitting to the straight line, the histogram highlights the presence of two island.

After the confirmation that the data are distributed normally, it is possible to analyse the factorial plan in detail.

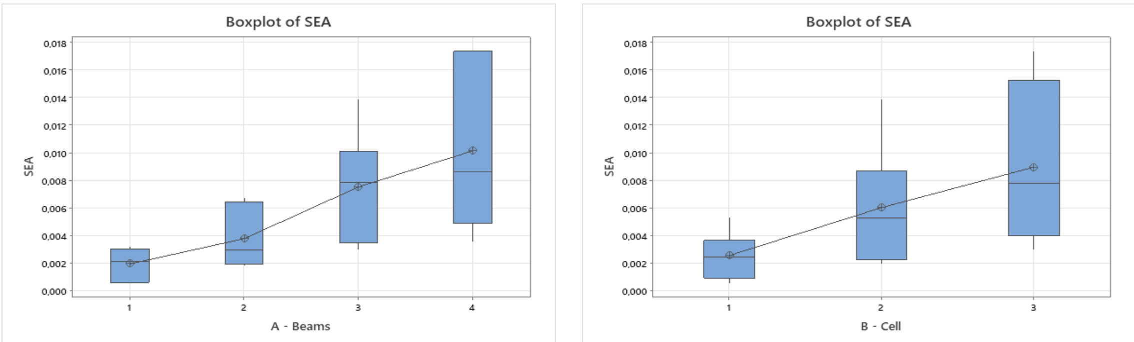


**FIGURE 2.10 - BOXPLOT OF FFP1 DATA**

Figure 2.10 shows the box plot of the experimental data: in particular the SEA is considered. The global trend seems to highlight the larger influence of factor A on the SEA, even if data must be further analysed more deeply in the following to better compare the influence of the factors.

The ANOVA was carried out with Minitab Software.

**Analysis of Variance**

| Source | DF | Seq SS | Contribution | Adj SS | Adj MS | F-Value | P-Value |
|---|---|---|---|---|---|---|---|
| Model | 11 | 0,000505 | 94,69% | 0,000505 | 0,000046 | 19,44 | 0,000 |
| Linear | 5 | 0,000410 | 76,97% | 0,000410 | 0,000082 | 34,77 | 0,000 |
| A - Beams | 3 | 0,000245 | 46,03% | 0,000245 | 0,000082 | 34,66 | 0,000 |
| B - Cell | 2 | 0,000165 | 30,94% | 0,000165 | 0,000082 | 34,95 | 0,000 |
| 2-Way Interactions | 6 | 0,000094 | 17,71% | 0,000094 | 0,000016 | 6,67 | 0,003 |
| A - Beams*B - Cell | 6 | 0,000094 | 17,71% | 0,000094 | 0,000016 | 6,67 | 0,003 |
| Error | 12 | 0,000028 | 5,31% | 0,000028 | 0,000002 | | |
| Total | 23 | 0,000533 | 100,00% | | | | |

**TABLE 2.6 – ANOVA OF FFP1 DATA**

Considering a confidence level of 0.5% ($\alpha = 0.005$), all the factors and the interactions included in the analysis are found to significantly affect the SEA, as represented by the data reported in Table 2.6. The Pareto Chart in Figure 2.11 shows this result graphically.

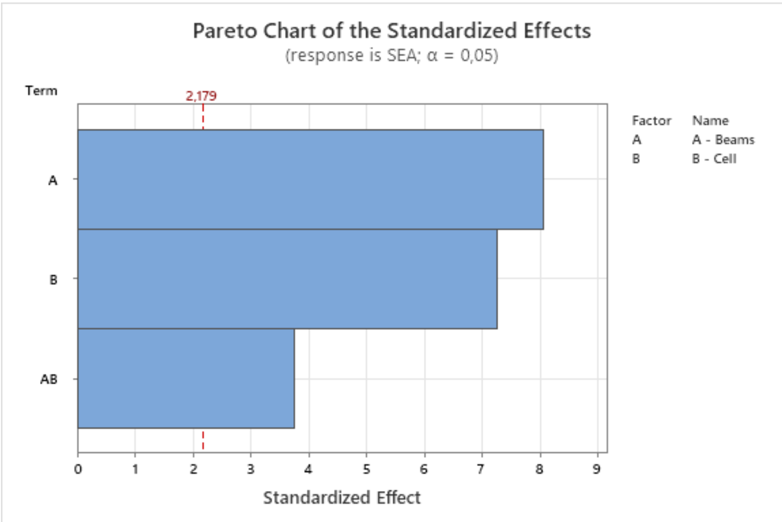


**FIGURE 2.11 – PARETO CHART OF FFP1 ANALYSIS**

According to Figure 2.11, factors A and B and their interaction have a large influence on the SEA. However, the interaction shows a smaller influence. Therefore, it can be concluded that once the volume of the structure is fixed, the diameter of the beams and the number of cell contribute in the same manner to the SEA increment.

# 2.2 Full factorial plan 2 (FFP2)

The procedure described in Section 2.1 before has been repeated and a second factorial plan, Full Factorial Plan 2 (FFP2), has been experimentally analysed. The goal of FFP2 is different from that of FFP1. Indeed, with FFP2, the lattice structure defined in [1] is directly replicated in space understanding which is the most influential factor for SEA, between beam diameter (Factor A) and cell number repetition (Factor B). Therefore, in this factorial plan a volume constraint has not set, and only the geometry of the lattice structure is fixed.

| | EA | SEA MAX | SEAavg | δIN | δend | MCF | PCF | CFE | EA | SEA MAX | SEAavg | δIN | δend | MCF | PCF | CFE |
|---|---|---|---|---|---|---|---|---|---|---|---|---|---|---|---|---|
| | J | J/mm3 | J/mm3 | mm | mm | [N] | [N] | [N/N] | J | J/mm3 | J/mm3 | mm | mm | [N] | [N] | [N/N] |
| **CELLA 01** | 1.77 | 0.0045 | 0.0038 | 5.53370 | 7.46370 | 273.54 | 399.58 | 68% | **1.27** | 0.0032 | **0.0028** | 6.28 | 7.89 | 198.41 | 289.77 | **68%** |
| | 0.76 | 0.0019 | 0.0018 | 7.03400 | 8.32400 | 123.29 | 179.95 | 69% | | | | | | | | |
| **CELLA 02** | 2.74 | 0.0026 | 0.0038 | 9.30465 | 13.00465 | 251.78 | 361.96 | 68% | **2.58** | 0.0023 | **0.0029** | 9.45 | 13.55 | 222.27 | 304.84 | **73%** |
| | 2.41 | 0.0021 | 0.0020 | 9.60414 | 14.10404 | 192.76 | 247.73 | 78% | | | | | | | | |
| **CELLA 03** | 3.69 | 0.0017 | 0.0017 | 10.00601 | 13.40601 | 304.37 | 438.38 | 69% | **4.28** | 0.0018 | **0.0018** | 10.01 | 14.16 | 316.91 | 457.91 | **69%** |
| | 4.87 | 0.0019 | 0.0019 | 10.00431 | 14.90431 | 329.45 | 477.44 | 69% | | | | | | | | |
| **CELLA 04** | 1.43 | 0.0023 | 0.0023 | 7.90410 | 8.65400 | 200.80 | 287.87 | 70% | **1.83** | 0.0028 | **0.0028** | 7.55 | 8.93 | 247.09 | 338.17 | **73%** |
| | 2.23 | 0.0034 | 0.0033 | 7.20460 | 9.20460 | 293.38 | 388.47 | 76% | | | | | | | | |
| **CELLA 05** | 6.37 | 0.0039 | 0.0037 | 6.90589 | 10.60589 | 590.79 | 827.80 | 71% | **5.17** | 0.0031 | **0.0030** | 7.81 | 11.46 | 484.55 | 691.38 | **70%** |
| | 3.96 | 0.0024 | 0.0023 | 8.70587 | 12.30587 | 378.30 | 554.96 | 68% | | | | | | | | |
| **CELLA 06** | 10.36 | 0.0029 | 0.0028 | 8.85625 | 12.82615 | 902.08 | 1264.99 | 71% | **13.04** | 0.0032 | **0.0031** | 10.01 | 14.07 | 957.94 | 1323.22 | **72%** |
| | 15.72 | 0.0035 | 0.0034 | 11.15504 | 15.30494 | 1013.81 | 1381.44 | 73% | | | | | | | | |
| **CELLA 07** | 7.45 | 0.0070 | 0.0065 | 7.40580 | 10.30580 | 973.64 | 1050.21 | 93% | **7.89** | 0.0069 | **0.0064** | 7.88 | 10.85 | 1025.61 | 1098.13 | **93%** |
| | 8.32 | 0.0069 | 0.0063 | 8.35360 | 11.40360 | 1077.57 | 1146.04 | 94% | | | | | | | | |
| **CELLA 08** | 22.57 | 0.0073 | 0.0068 | 12.20481 | 15.37991 | 1959.20 | 1722.16 | 88% | **35.56** | 0.0112 | **0.0104** | 12.15 | 15.69 | 3264.99 | 2953.96 | **90%** |
| | 48.55 | 0.0151 | 0.0139 | 12.10430 | 16.00110 | 4570.77 | 4185.75 | 92% | | | | | | | | |
| **CELLA 09** | 58.31 | 0.0077 | 0.0075 | 16.55070 | 19.53070 | 3730.11 | 3620.15 | 97% | **51.94** | 0.0079 | **0.0077** | 14.20 | 17.09 | 3680.19 | 3576.61 | **97%** |
| | 45.57 | 0.0080 | 0.0078 | 11.85600 | 14.65600 | 3630.27 | 3533.06 | 97% | | | | | | | | |
| **CELLA 10** | 13.38 | 0.0096 | 0.0092 | 8.30380 | 9.78370 | 1934.83 | 1920.74 | 99% | **13.28** | 0.0094 | **0.0090** | 8.43 | 9.94 | 1906.59 | 1876.90 | **98%** |
| | 13.19 | 0.0092 | 0.0088 | 8.56600 | 10.10590 | 1878.36 | 1833.05 | 98% | | | | | | | | |
| **CELLA 11** | 35.79 | 0.0093 | 0.0088 | 11.99862 | 14.29862 | 3949.08 | 4012.82 | 98% | **35.88** | 0.0093 | **0.0086** | 11.58 | 14.33 | 3974.98 | 3920.17 | **97%** |
| | 35.98 | 0.0093 | 0.0085 | 11.16123 | 14.37123 | 4000.88 | 3827.52 | 96% | | | | | | | | |
| **CELLA 12** | 118.12 | 0.0103 | 0.0096 | 18.36883 | 22.15883 | 8633.24 | 8103.06 | 94% | **119.46** | 0.0108 | **0.0102** | 17.88 | 21.40 | 8778.19 | 8196.46 | **93%** |
| | 120.79 | 0.0113 | 0.0107 | 17.39976 | 20.64976 | 8923.13 | 8289.85 | 93% | | | | | | | | |

**TABLE 2.7 - TEST RESULTS OF FACTORIAL PLAN 2**

Table 2.7 reports the results of the experimental tests and the corresponding parameters useful to analyse the performances of the structures.

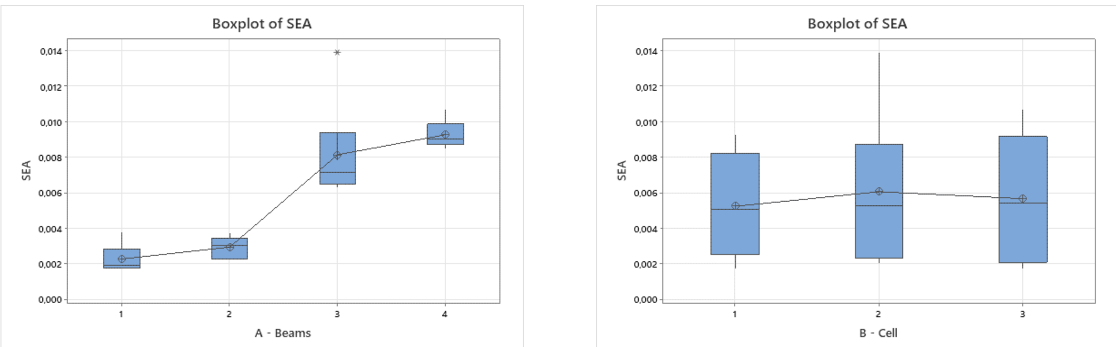


**FIGURE 2.12 – BOXPLOT OF FFP2 DATA**

Also, for this factorial plan is convenient to organize the data in a box plot, here reported in Figure 2.12. Factor A has a similar trend as in factorial plan 1, instead the factor B shows a different tendency. Indeed, the average value of SEA at level 2 is the highest, proving that the efficiency of the SEA can be reached with the configuration at level 2 (3x3 configuration).

The normality of the data related to each factor is verified through the Normality Plots represented in Figure 2.13. The experimental point showing the SEA significantly larger than the SEA of the other experimental data can be considered an outlier. According to this, it is removed, and the cumulated data better fit the straight line of the Normality Plot, as shown in Figure 2.14.

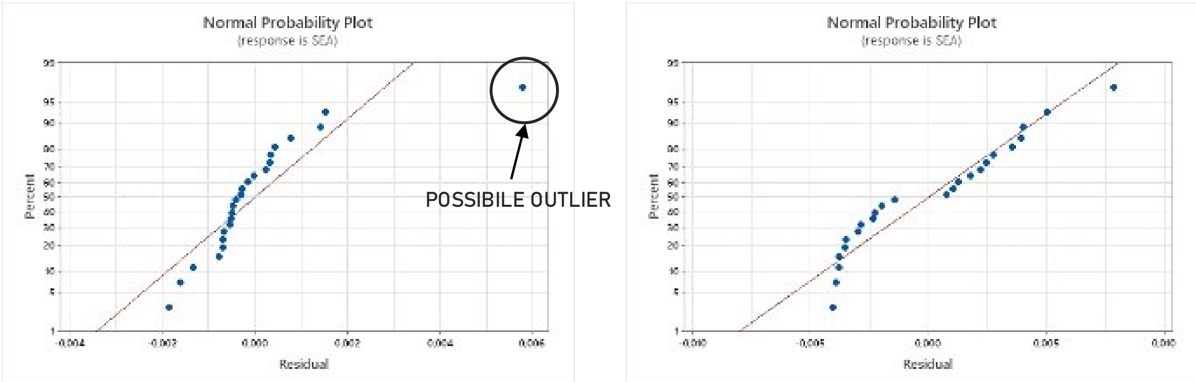


**FIGURE 2.13 - NORMALITY PLOT OF FFP2 DATA**

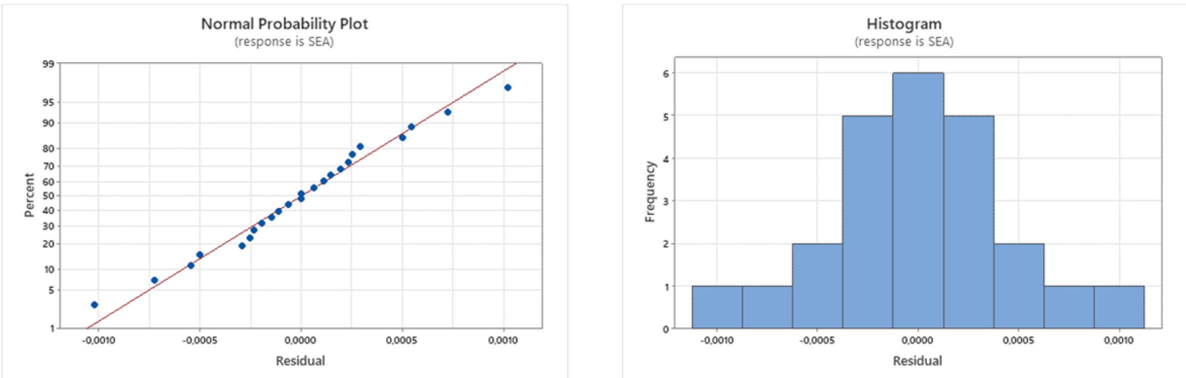


**FIGURE 2.14 - NORMALITY PLOT AND HISTOGRAM (OUTLIER REMOVAL)**

In addition, in Figure 2.14, it is represented also the data grouped in a histogram form useful to appreciate the well-fitting to a gaussian distribution.

An ANOVA analysis has been thereafter performed, to assess the influence of the investigated factors for these configurations.

## Analysis of Variance

| Source | DF | Seq SS | Contribution | Adj SS | Adj MS | F-Value | P-Value |
|---|---|---|---|---|---|---|---|
| Model | 11 | 0,000205 | 97,71% | 0,000205 | 0,000019 | 46,56 | 0,000 |
| Linear | 5 | 0,000201 | 95,81% | 0,000201 | 0,000040 | 100,44 | 0,000 |
| A - Beams | 3 | 0,000200 | 95,26% | 0,000200 | 0,000067 | 166,44 | 0,000 |
| B - Cell | 2 | 0,000001 | 0,55% | 0,000001 | 0,000001 | 1,44 | 0,276 |
| 2-Way Interactions | 6 | 0,000004 | 1,90% | 0,000004 | 0,000001 | 1,66 | 0,214 |
| A - Beams*B - Cell | 6 | 0,000004 | 1,90% | 0,000004 | 0,000001 | 1,66 | 0,214 |
| Error | 12 | 0,000005 | 2,29% | 0,000005 | 0,000000 | | |
| Total | 23 | 0,000209 | 100,00% | | | | |

**TABLE 2.8 – ANOVA OF FFP2 DATA**

By considering a confidence level of 0.5% ($\alpha = 0.005$), the P-value highlight that only factor A significantly affect the SEA. As before, also the Pareto Chart shown in Figure 2.15, was considered to verify the contribution of the investigated factors on SEA graphically.

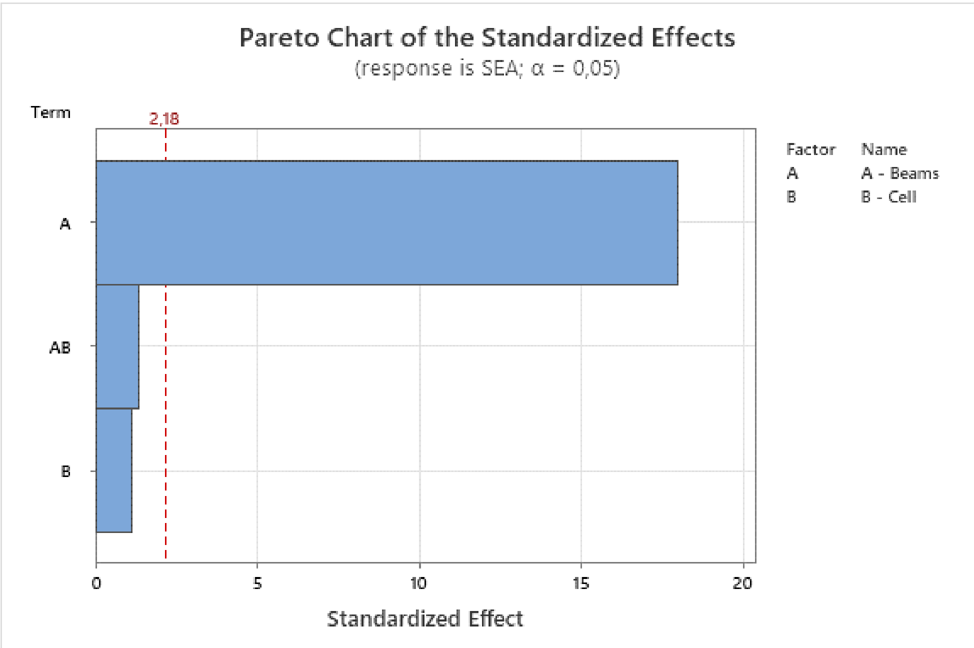


**FIGURE 2.15 - PARETO CHART OF FFP2**

As already stated, only factor A, i.e. the diameter of the internal beams, has a significant influence on SEA. In fact, according to Table 2.7, an increment of the diameters of the beams induce an increment of energy absorbed and SEA. Instead, for factor B, the trend is much different, because passing from a configuration 2x2 to a 3x3 not always is convenient. For example, fixing the diameter to Ø1.8, the SEA decrease of about 4%.

Furthermore, by assuming that lattice structures can be represented by several springs that work in series or parallel, experimental data show the following trends:

- Increasing the number of layers (i.e. springs that work in series), the overall stiffness of the structure decreases, increasing the global displacement.
- Increasing the number of cells for each layer (i.e. springs that work in parallel), the stiffness of the structure increase decreasing the global displacement.

Therefore, from this point of view, if the objective is to absorb the energy during a crash more efficiently, it is convenient to increase the number of structures within a layer and increase as much as possible the diameter of the internal beams. On the contrary, if the objective is to decrease the deceleration after an impact the number of layers should be increase and the diameter of the beams should be adapted in order to guarantee a progressive reaction.

Obviously, for completeness and accuracy, the data will be analysed to select the most efficient structure for the design of the crashbox including also the possible outlier. This is because additive manufacturing process is affected by a large intrinsic variability, so it could be expected that the test result excluded previously can be included in the analysis. In this case, by considering the SEA, the most efficient structure is the 08. However, by comparing the value of SEA, it is clear that the difference between structures 08 and 12 is not so large. Therefore, for a better comparison, the maximum absorbed energy and CFE should be included in the analysis. Accordingly, the best performances can be obtained with structure 12.

# 2.3 Lattice structure for crash box design

To define the best configuration for a crash box the attention should focus on the analysis of the CFE, SEA and EA parameters. Accordingly, three structures can be considered for a crash box:

| | EA | SEA MAX | SEAavg | δIN | δend | MCF | PCF | CFE |
|---|---|---|---|---|---|---|---|---|
| | J | J/mm3 | J/mm3 | mm | mm | [N] | [N] | [N/N] |
| **CELLA 8** | **35.56** | 0.0112 | **0.0104** | 12.15 | 15.69 | 3264.99 | 2953.96 | **90%** |
| **CELLA 12 FFP2** | **119.46** | 0.0108 | **0.0102** | 17.88 | 21.40 | 8778.19 | 8196.46 | **93%** |
| **CELLA 12 FFP1** | **90.05** | 0.0184 | **0.0174** | 10.50 | 12.00 | 13552.76 | 14049.50 | **96%** |

**TABLE 2.9 - MOST EFFICIENT LATTICE STRUCTURE COMPARISON**

It is also important to analyse the mechanical response of the lattice structures reported in Table 2.9, in order to take into consideration also the collapsing mode of the structures.

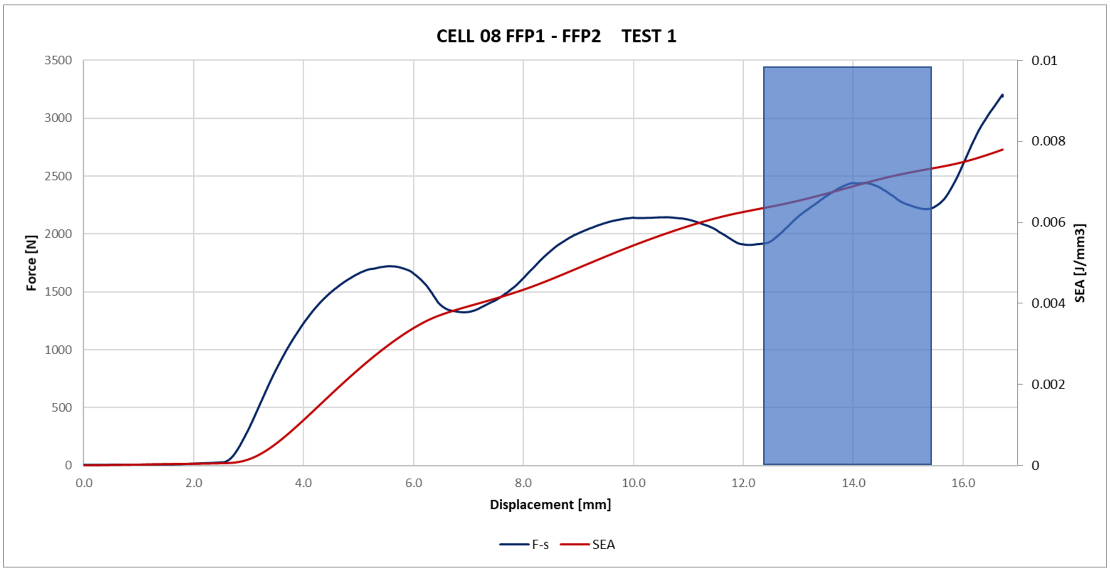


**FIGURE 2.16 - EXPERIMENTAL TEST CELL 08 FFP1-FFP2 TEST 1**

| EA | SEA MAX | $SEA_{avg}$ | $\delta_{IN}$ | δend | MCF | PCF | CFE |
|---|---|---|---|---|---|---|---|
| J | J/mm3 | J/mm3 | mm | mm | [N] | [N] | [N/N] |
| **22.57** | **0.0073** | **0.0068** | 12.20 | 15.38 | 1957.87 | 2441.13 | 80% |

**TABLE 2.10 - RESULTS OF CELL 08 FFP1 - FFP2 TEST 1**

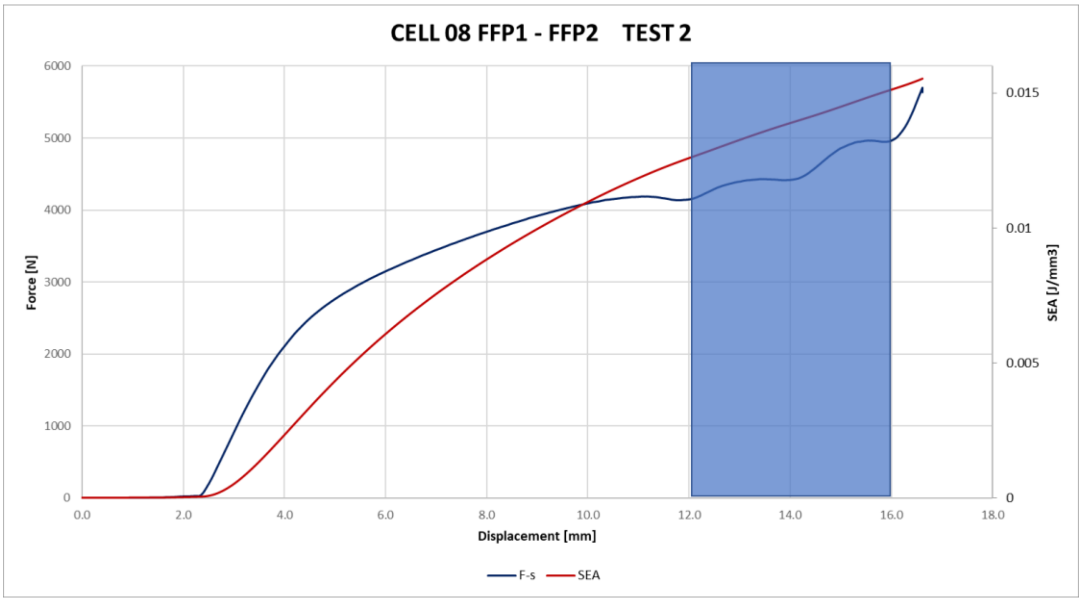


**FIGURE 2.17 - EXPERIMENTAL TEST CELL 08 FFP1 - FFP2 TEST 2**

| EA | SEA MAX | $SEA_{avg}$ | $\delta_{IN}$ | $\delta$end | MCF | PCF | CFE |
|---|---|---|---|---|---|---|---|
| J | J/mm3 | J/mm3 | mm | mm | [N] | [N] | [N/N] |
| 48.55 | 0.0151 | 0.0139 | 12.10 | 16.00 | 4463.05 | 4963.90 | 90% |

**TABLE 2.11 - RESULTS OF CELL 08 FFP1 - FFP2 TEST 2**

Figure 2.16 and Figure 2.17 show the mechanical response of structure 08 in the two different compressive tests performed. Here, in Table 2.10 and Table 2.11, the main parameters useful to compare the structure are reported. Therefore, considering the differences shown in the two tests, the lattice structure 08 suggests a large dispersion of the results that could be assessed to the intrinsic variability of the additive manufacturing process. For this structure, three local collapses associated to a load drop of the force are visible. In the case of test 2 (Figure 2.17) the load drops are small, consequently a high CFE results. For test 1, instead, the load drops are more evident causing a decrement in CFE of 20%. The overall trends of the load, in the two performed tests, are continuously increasing up to densification recalling in such a way the foam characteristics without showing an evident plateau.

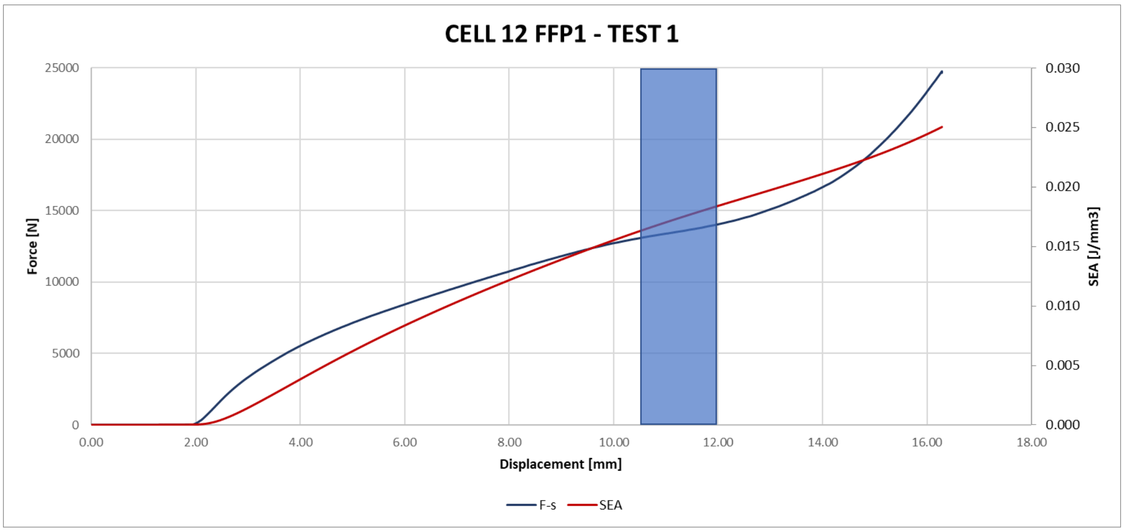


**FIGURE 2.18 - EXPERIMENTAL TEST CELL 12 FFP1 TEST 1**

| EA | SEA MAX | $SEA_{avg}$ | $\delta_{IN}$ | δend | MCF | PCF | CFE |
|---|---|---|---|---|---|---|---|
| **J** | **J/mm3** | **J/mm3** | **mm** | **mm** | **[N]** | **[N]** | **[N/N]** |
| **90.05** | **0.0184** | **0.0174** | 10.50 | 12.00 | 13552.76 | 14049.50 | 96% |

**TABLE 2.12 - RESULTS OF CELL 12 FFP1 TEST 1**

Figure 2.18 and Table 2.12 refer to the test performed on structure 12 FFP1. The relative high-volume density of this lattice structure positively affects the collapsing mode. In fact, carbon nylon mechanical properties and the high stiffness of the structure guarantees for this configuration a mechanical curve very similar to that of a foam. The plateau is not so evident, but a small region with quite constant force can be found between 10.50 and 12.00 mm. The compression instability is never reached for this configuration, because large load drops are not evident, guarantying a very high efficiency and absorbed energy. Obviously, the main disadvantage of this layout is the high amount of energy absorbed in a low volume, i.e., a very steep deceleration is expected.

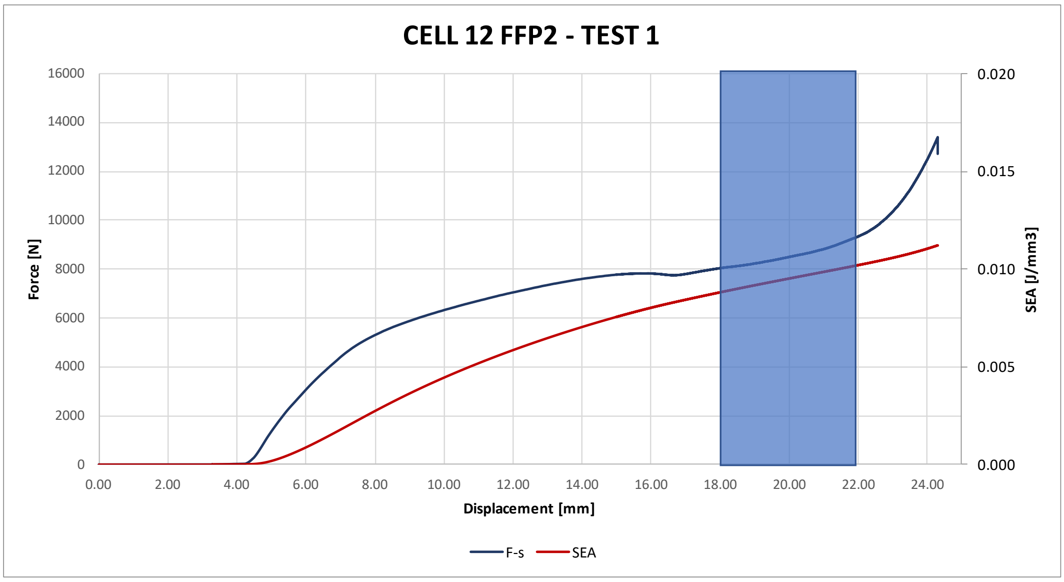


FIGURE 2.19 - EXPERIMENTAL TEST CELL 12 FFP2 TEST 1

| EA | SEA MAX | $SEA_{avg}$ | $\delta_{IN}$ | δend | MCF | PCF | CFE |
|---|---|---|---|---|---|---|---|
| J | J/mm3 | J/mm3 | mm | mm | [N] | [N] | [N/N] |
| 118.12 | 0.0103 | 0.0096 | 18.37 | 22.16 | 8633.24 | 8103.06 | 94% |

TABLE 2.13 - RESULTS OF CELL 12 FFP2 TEST 1

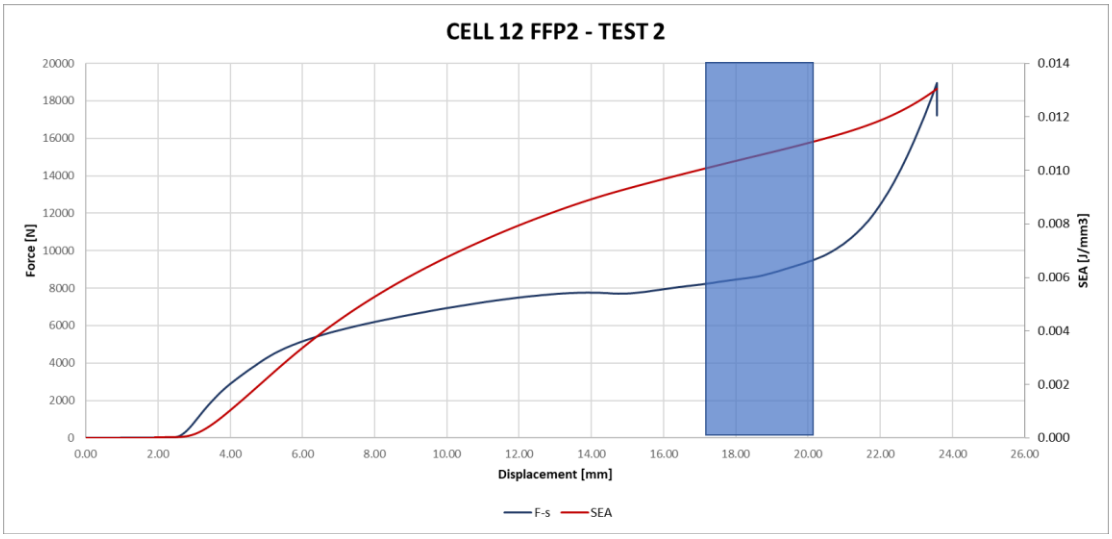


FIGURE 2.20 - EXPERIMENTAL TEST CELL 12 FFP2 TEST 2

| EA | SEA MAX | $SEA_{avg}$ | $\delta_{IN}$ | δend | MCF | PCF | CFE |
|---|---|---|---|---|---|---|---|
| J | J/mm3 | J/mm3 | mm | mm | [N] | [N] | [N/N] |
| 120.79 | 0.0113 | 0.0107 | 17.40 | 20.65 | 8923.13 | 8289.85 | 93% |

TABLE 2.14 - RESULTS OF CELL 12 FFP2 TEST 2

Figure 2.19 and Figure 2.20 include the mechanical response of structure 12 for the two tests performed. Table 2.13 and Table 2.14 report the main parameters associated to these tests. The force versus displacement curve, in both tests, shows in this case an extended plateau due to the large available volume with respect the cell FFP1. However, as already stated, a larger dimension of the unit lattice structure means a lower stiffness and a decrease of SEA. The extension of the plateau surely guarantee that a certain amount of energy can be absorbed in a higher volume resulting in a smoother deceleration after impact.

| | SEA | STIFFNESS | DECELERATION | CFE |
|---|---|---|---|---|
| LAYER ↑ | - | - | ++ | = |
| Ø BEAM ↑ | + | + | - | ++ |
| CELL per LAYER ↑ | ++ | ++ | -- | = |

**FIGURE 2.21 - CORRELATION MATRIX BETWEEN FACTORS INCREMENTS AND EFFECTS**

To conclude the experimental activity, with the main design target to maximize the specific energy absorption, the most efficient structure to be used as the base of our crash box is the lattice structure 12 FFP1 (Ø1.8 mm – 4x4 configuration). For sure, in the following chapters, the design criteria evaluated with the factorial plans analysis must be taken always in mind, especially for what concern the results of FFP2. In fact, to avoid a loss of efficiency as the number of layers of the crash box increases a variable beams structure capable to guarantee a uniform reaction to the crash is to be considered. Here, in Figure 2.21, is reported in a graphical form the relation between factors increments and their consequent effects. It results to be efficient to summarize the all the key concepts evaluated with the experimental activity.

# CHAPTER 3

# Finite Element Analysis (FEA)

This chapter has the aim to present the FEM and its correlation with respect to the experimental data. Obviously, the structure on which the attention will be focus is the Cell 12 FFP1 that represents the base for the design of the crash box.

## 3.1 Finite element method (FEM) model

The FEM model of the Cell 12 FFP1 will be analysed in more detail in this section and the attention will be focused on the modelling of the contacts included in the model, particularly. As a first attempt, only an AUTOMATIC_SINGLE_SURFACE contact is implemented in order to manage both the interactions between the RWALL and the lattice structure and the self-contact of the lattice beams. Figure 3.1 reports the comparison of the experimental and numerical results where the AUTOMATIC_SINGLE_SURFACE contact is considered. As shown, the discrepancy is quite significant, mainly due to an unrealistic interpenetration between lattice beams.

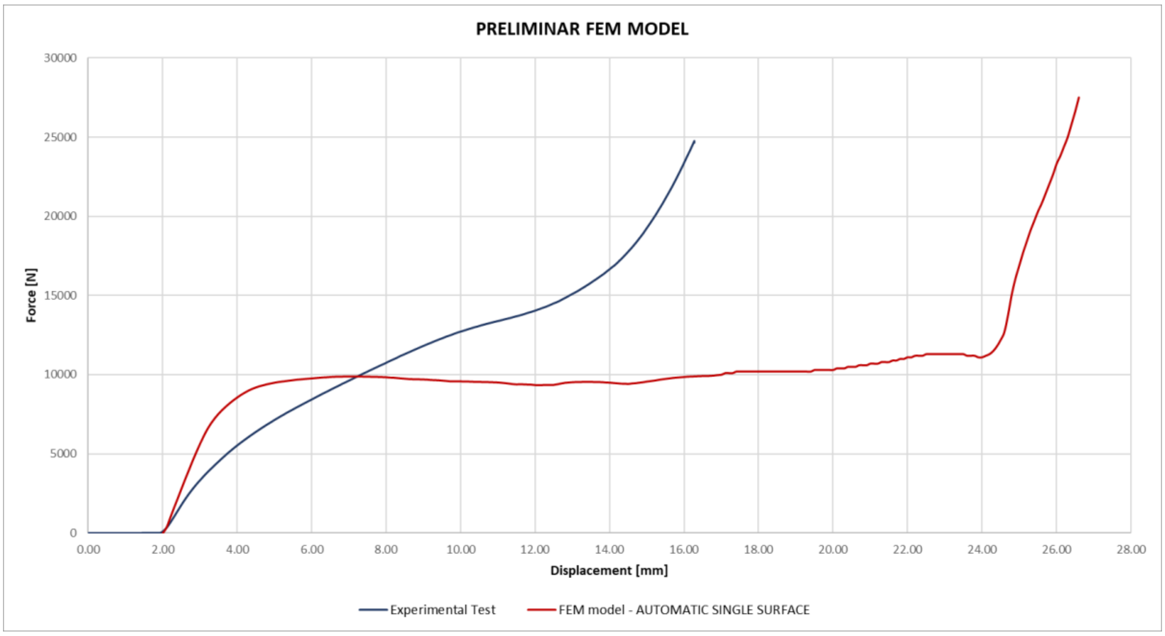


**FIGURE 3.1 - FEM MODEL CELL 12 FFP1 - AUTOMATIC SINGLE SURFACE**

The numerical deformation is rather extended with respect to the experimental data because of the interpenetration between internal beams. However, comparing experimental and numerical results of the other lattice structures tested for the development of the factorial plans, it is understood that material, property and boundary conditions are well defined because the model can lead to the correct estimation of the average load and deformation mechanism. To improve the correlation, a new version of the FEM model is developed with the addition of a different contact formulation for internal beams contact.

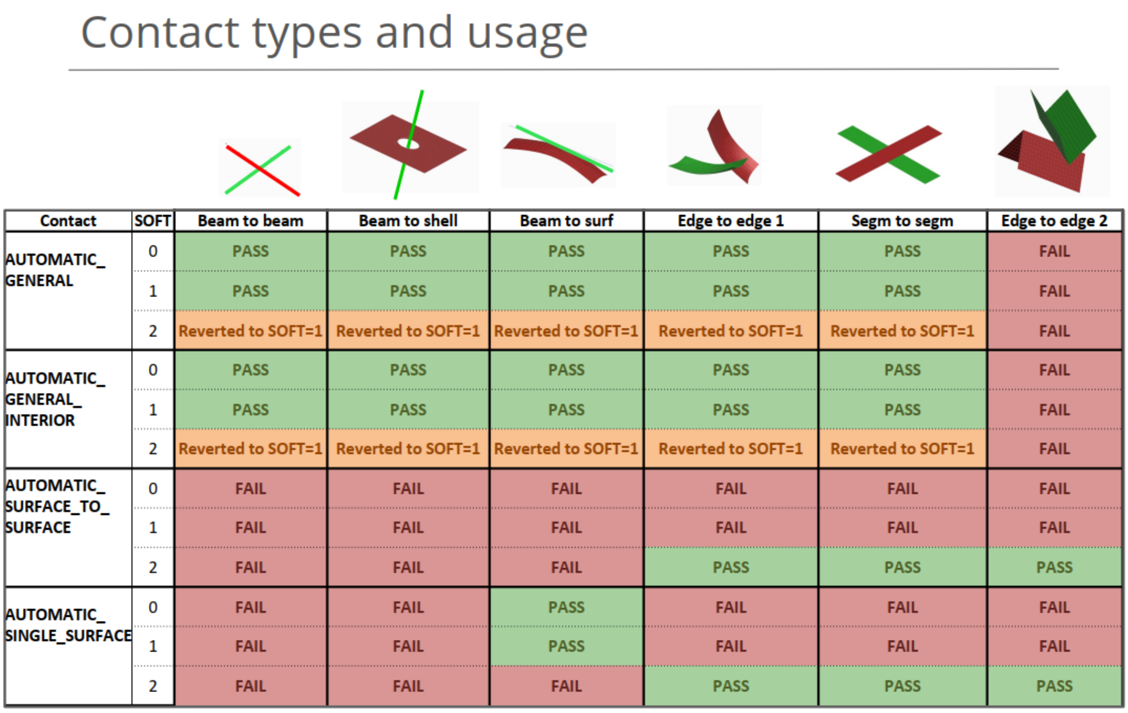

Contact types and usage

| Contact | SOFT | Beam to beam | Beam to shell | Beam to surf | Edge to edge 1 | Segm to segm | Edge to edge 2 |
|---|---|---|---|---|---|---|---|
| AUTOMATIC_ GENERAL | 0 | PASS | PASS | PASS | PASS | PASS | FAIL |
| | 1 | PASS | PASS | PASS | PASS | PASS | FAIL |
| | 2 | Reverted to SOFT=1 | Reverted to SOFT=1 | Reverted to SOFT=1 | Reverted to SOFT=1 | Reverted to SOFT=1 | FAIL |
| AUTOMATIC_ GENERAL_ INTERIOR | 0 | PASS | PASS | PASS | PASS | PASS | FAIL |
| | 1 | PASS | PASS | PASS | PASS | PASS | FAIL |
| | 2 | Reverted to SOFT=1 | Reverted to SOFT=1 | Reverted to SOFT=1 | Reverted to SOFT=1 | Reverted to SOFT=1 | FAIL |
| AUTOMATIC_ SURFACE_TO_ SURFACE | 0 | FAIL | FAIL | FAIL | FAIL | FAIL | FAIL |
| | 1 | FAIL | FAIL | FAIL | FAIL | FAIL | FAIL |
| | 2 | FAIL | FAIL | FAIL | PASS | PASS | PASS |
| AUTOMATIC_ SINGLE_SURFACE | 0 | FAIL | FAIL | PASS | FAIL | FAIL | FAIL |
| | 1 | FAIL | FAIL | PASS | FAIL | FAIL | FAIL |
| | 2 | FAIL | FAIL | FAIL | PASS | PASS | PASS |

**FIGURE 3.2 – LS-DYNA CONTACT FORMULATION COMPARISON**

Figure 3.2, taken from the webinar presentation *"LS-DYNA Introduction to contacts"*[3] compares all the possible contact formulations useful for this work. The contact formulation AUTOMATIC_SINGLE_SURFACE does not guarantee the BEAM-TO-BEAM contacts, so the need to implement AUTOMATIC_GENERAL formulation is crucial.

In order to implement this kind of contact, a duplicated lattice structure merged to the original one has been created. In this way, it is possible to define one beam structure for the evaluation of the structural response and the other it is used only to manage the self-contact between beams. Therefore, through the assignment of a MAT_NULL material formulation to the duplicated structure, it is possible to set parameters in order to correctly

[3] *"LS-DYNA Introduction to contacts" - Emily Owen (Oasys) – [Jan 2020]*

define the self-contact between the beams. The parameters were optimized through an iterative procedure in order to improve the correlation of the force versus displacement chart obtained from the experimental test done. A summary of the main parameters is presented below in Table 3.1.

| FEM | Ø NULL BEAM [mm] | Ø BEAM [mm] | GENERAL FRICTION COEFFICIENT [-] | BASE RWALL FRICTION COEFFICIENT [-] | YOUNG MODULUS (MAT_NULL) [MPa] | YOUNG MODULUS (MAT_BEAM) [MPa] |
|---|---|---|---|---|---|---|
| CELL 12 FFP1 | 1.80 | 1.65 | 0.10 | 0.30 | 10 000 | 3510.62 |

**TABLE 3.1 - CONTACT PARAMETERS CELL 12 FFP1**

So, the diameter and Young Modulus of the elements related to MAT_NULL are used in order to model correctly the real contact behaviour of the structure.

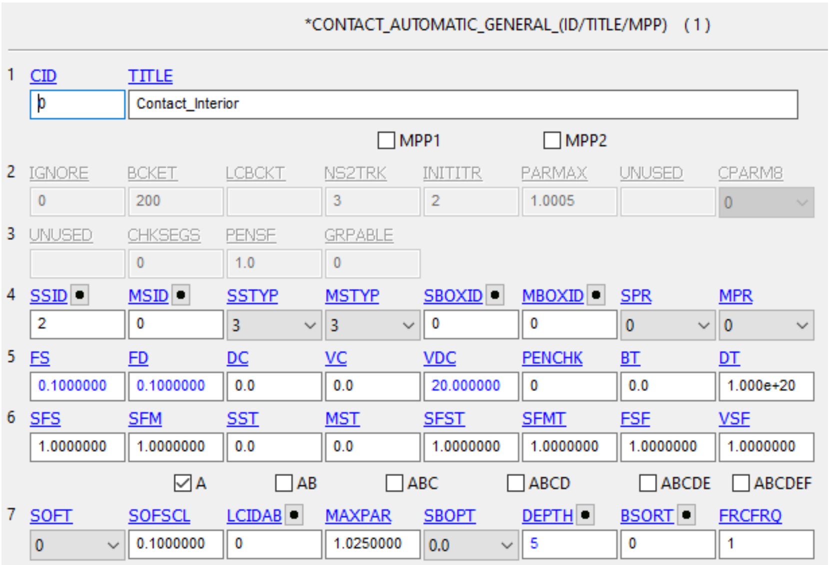


**FIGURE 3.3 - CONTACT AUTOMATIC_GENERAL DEFINITION**

Another important feature of the FEM model, which requires particular attention to properly estimate the mechanical performances of the structure, is the diameter of the beams assigned to the standard property SECTION_BEAM. Indeed, due to the large variability of the additive manufacturing process, the resulting diameter of the beams can be very different from what designed through the CAD model. So, during the experimental tests, measurements of the effective diameter of the beams were performed through an electronic system of acquisition with image magnification and also with SEM microscope (Scanning Electron Microscope).

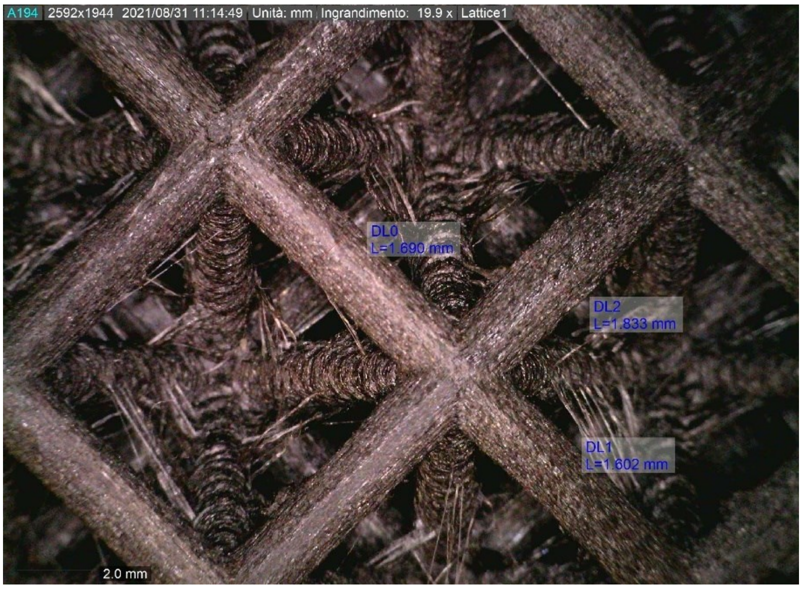


**FIGURE 3.4 - DIAMETER MEASUREMENT WITH IMAGE MAGNIFICATION**

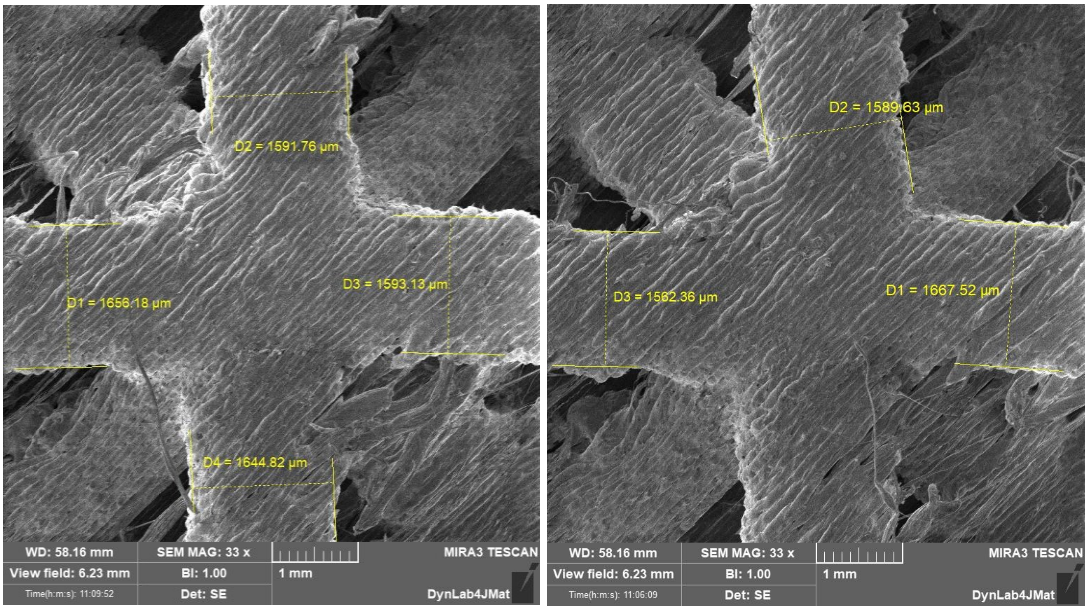


**FIGURE 3.5 - DIAMETER MEASUREMENT WITH SEM**

From these measurements an effective average diameter of about 1.65 mm is used as reference for a beam's diameter of 1.8 mm.

## 3.2 FEA correlation results of lattice 12 FFP1

Figure 3.6 shows the comparison of the experimental and numerical results for the lattice structure 12 FFP1. A very good agreement can be appreciated.

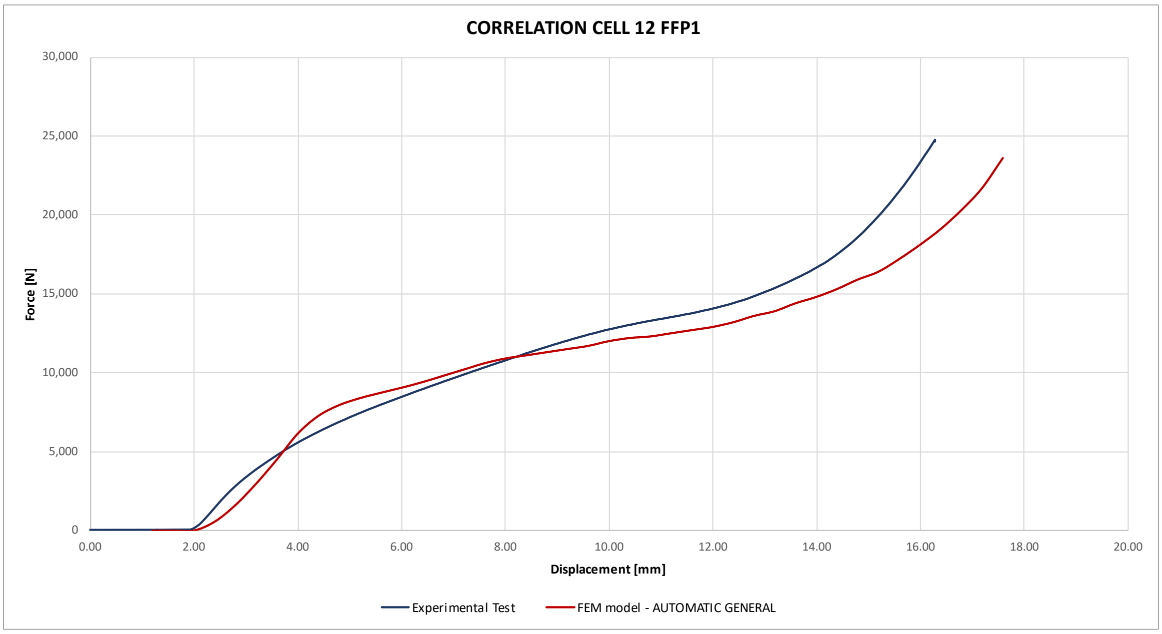


**FIGURE 3.6 - FEA FORCE-DISPLACEMENT CORRELATION CELL 12 FFP1**

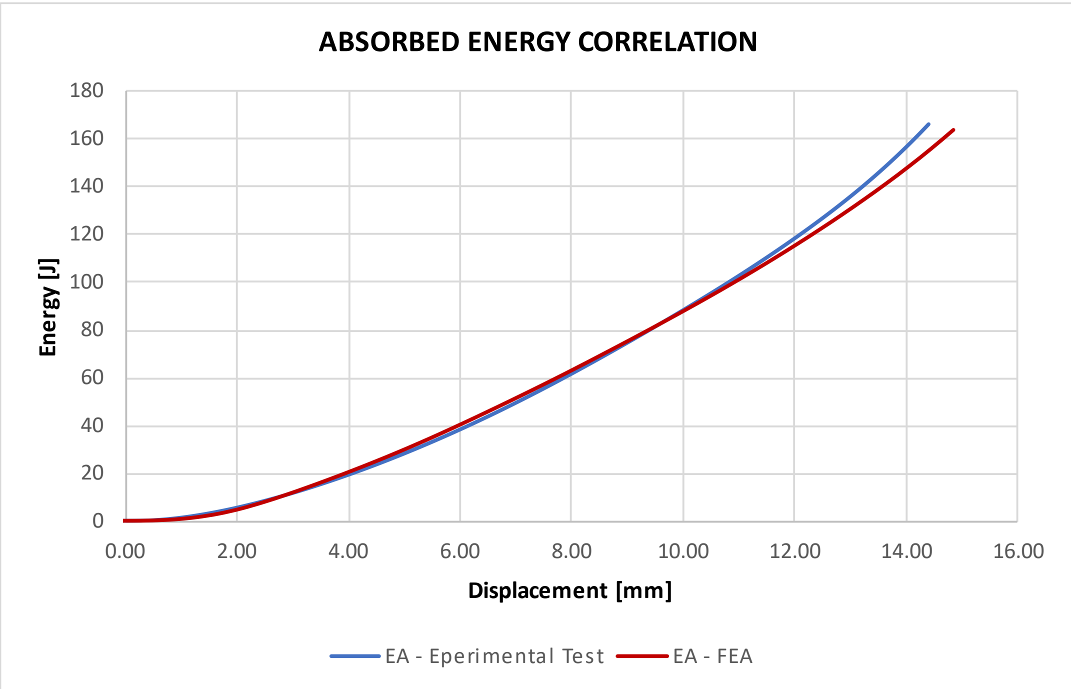


**FIGURE 3.7 - FEA ENERGY CORRELATION CELL 12 FFP1**

Performing the integral of the force-displacement curves it is possible to evaluate the absorbed energy as function of the displacement, as represented in Figure 3.7. Regarding the energy, a discrepancy of 4% is achieved at the end of the experimental test, which reduces to 3% just before the densification.

The very good agreement between the experimental and numerical results can be appreciated also through the collapsing mode shown by the structure in the compressive test. The comparison between the experimental and numerical collapsing mode is shown in Figure 3.8. In particular, the effective plastic strain contour plot is shown.

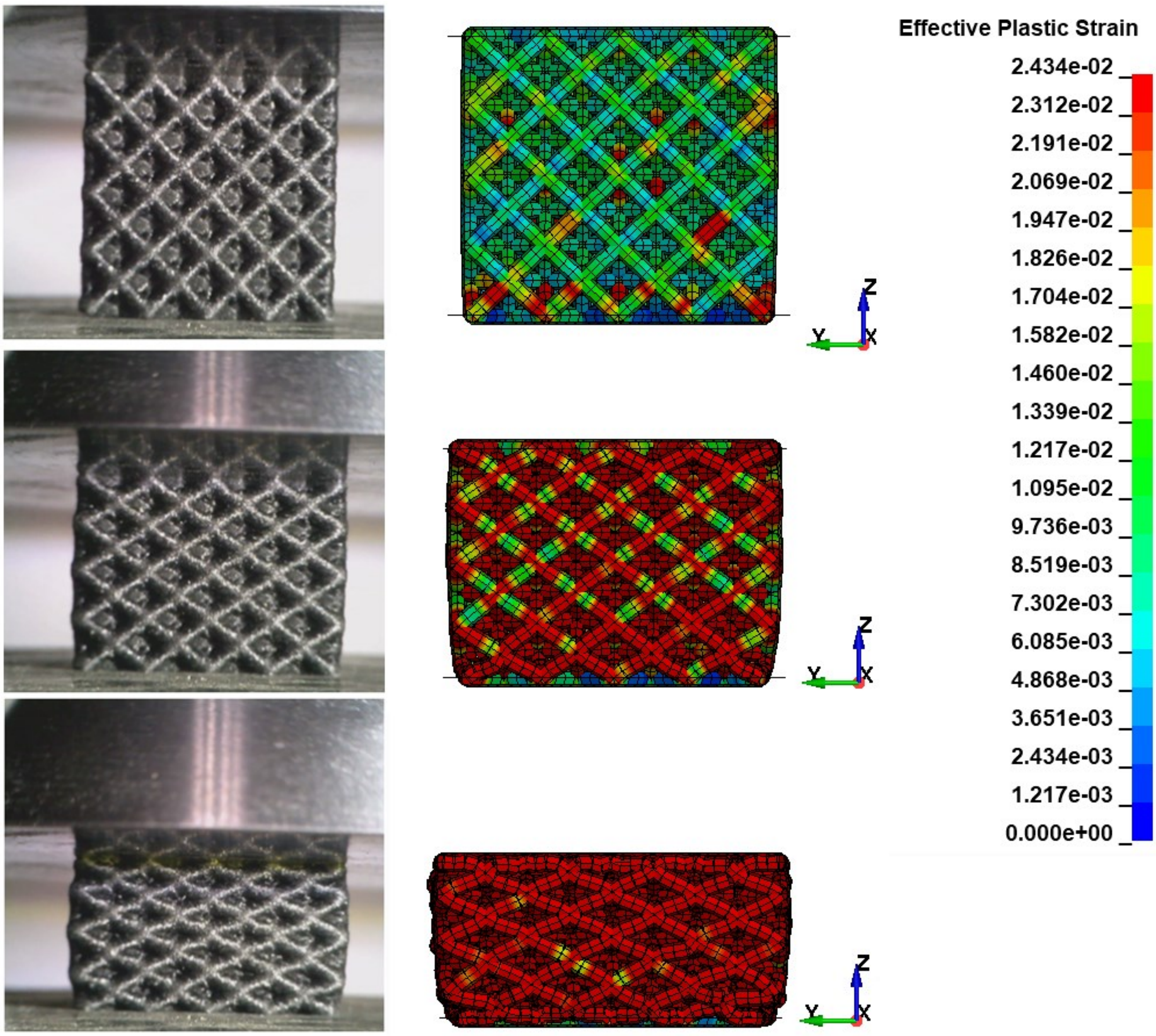


**FIGURE 3.8 - DEFORMATION SEQUENCE OF CELL 12 FFP1**

The collapsing mode of the lattice structure is estimated well by the FEM model. The layers are continuously compressed until densification occurs. The sequence of collapsing founded experimentally is replicated exactly by the simulation. In fact, the top and bottom parts, which are directly in contact with the testing planes are the first parts of the structure to collapse. Then the structure shows a gradual compression of the entire component up to densification. The high efficiency of this structure is highlighted through the plastic strain flow. From the first frames of the compression test, the whole structure immediately yields, as shown in the top figure on the right. Therefore, thanks to the peculiar geometrical configuration, the whole material of the lattice structure is strongly involved in the compression, thus highlighting the high effectiveness of this structure, even from the very first instant of the compression.

# CHAPTER 4

# AM Crash Box Design

In this chapter the design procedure of the different versions of the AM crash box will be presented. The component will be evaluated and designed in comparison with the Toyota Yaris's crash box, in order to have a real-world component reference.

## 4.1 Target setting

Starting from the targets definition of the AM crash box, it is needed to know that its principal goal is to absorb the kinetic energy coming from a low speed frontal crash. Indeed, the crash box is a structure designed to avoid that the components of the front frame will be deformed during a crash at low speed. In this way, for crashes of weak entity, longitudinal members and ancillaries components are not get involved into the deformation. This led to a decrease of repairs costs after a crash that requires amount of energy to be absorbed of much lower value compared to a traditional frontal crash at 50-56 km/h.

For reference, the test procedure to assess a vehicle's damageability and repairability is included into RCAR low-speed structural crash test protocol and it includes the following impacts:

- 15 km/h frontal impact into a rigid barrier.
- 15 km/h rigid-faced mobile barrier rear impact.

This protocol is encouraging vehicle designers to limit unnecessary damage to the structure of passengers vehicles in low speed impacts. Even though this protocol refers to the full vehicle impact, it will be here assumed as the reference for the design of the lattice crash box.

The layout of the frontal test included into the appendix 1 of the RCAR low-speed structural crash test protocol[4] is reported in Figure 4.1.

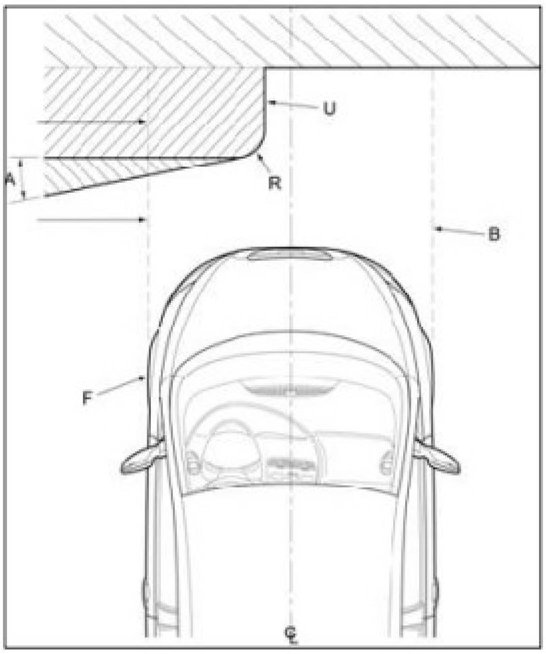


**FIGURE 4.1 - RCAR FRONT RIGID BARRIER IMPACT PROTOCOL (40% OVERLAP)**

In order to replicate the RCAR low-speed crash test protocol, it is firstly necessary to identify the target energy to be absorbed by the crash box. Once, the test is performed with a 40% of overlap, it means that all the kinetic energy associated to the speed of the vehicle must be absorbed by only one component. Besides, it is also convenient to consider that the crash box alone is capable to absorb all the energy of the impact neglecting the contribution of the bumper itself.

Considering a C-segment vehicle with a mass of 1360 kg and travelling at a speed of 15 km/h (+1/-0) as requested by the protocol, it is possible to evaluate the kinetic energy to be absorbed as:

$$E_{ins} = \frac{1}{2} m\, V_{ins}^2 = 11.8\ kJ \tag{4.1}$$

In addition, it could be convenient to limit the average load to 220 kN to limit the resultant acceleration to which the passengers will be subjected to.

[4] *RCAR (Research Council for Automotive Repairs) – [July 2011]*

To assume a more realistic design scenario, the crash box adopted in the Toyota Yaris, is considered, where also the geometrical constraints in terms of envelope are taken into account. So, a box volume of dimensions 235 x 89 x 109 mm (X – Y – Z), that is the maximum available envelope in the Toyota Yaris, is set as reference (Figure 4.2).

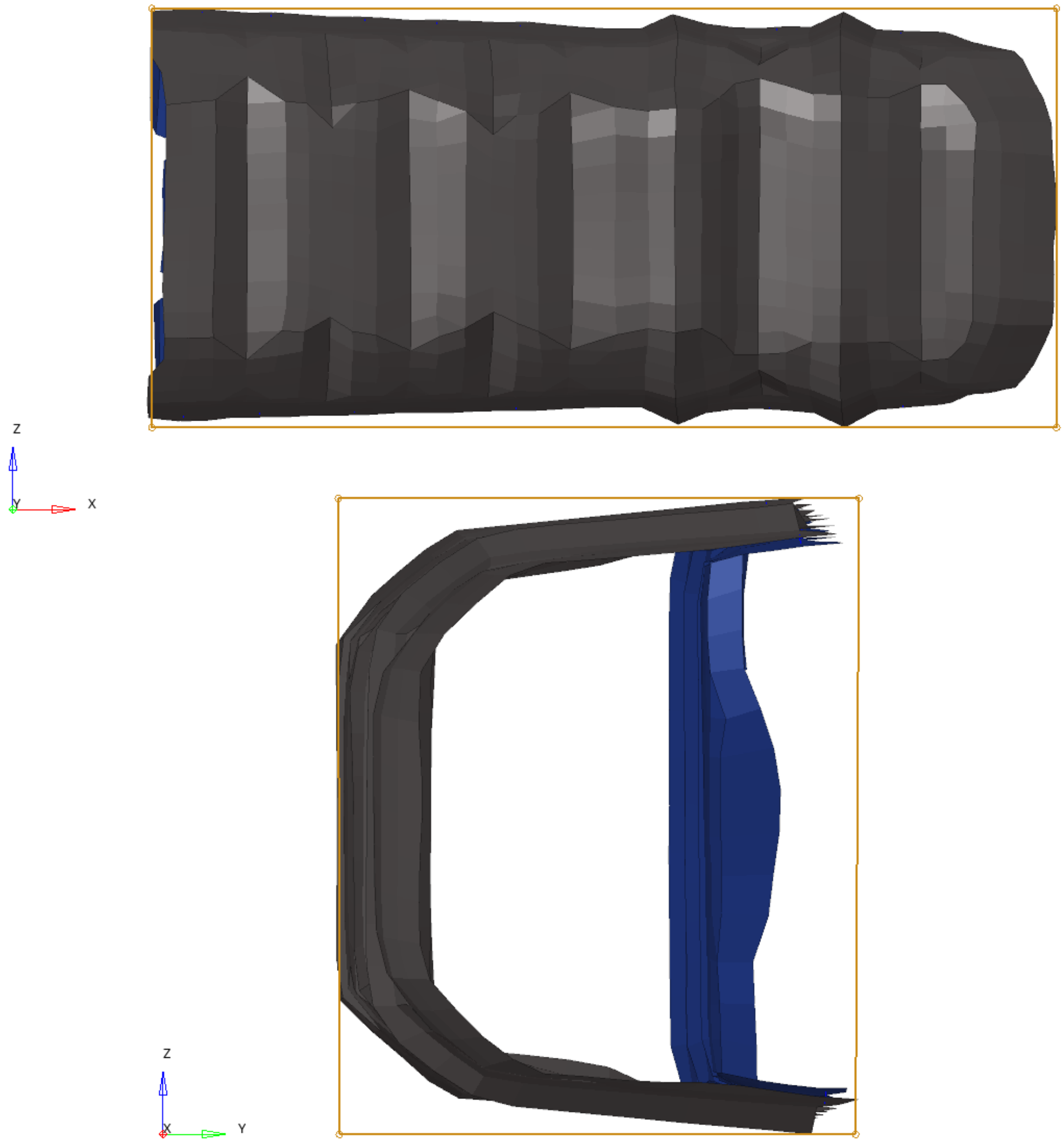


**FIGURE 4.2 - CRASH BOX'S MAXIMUM ENVELOPE (ZX – ZY)**

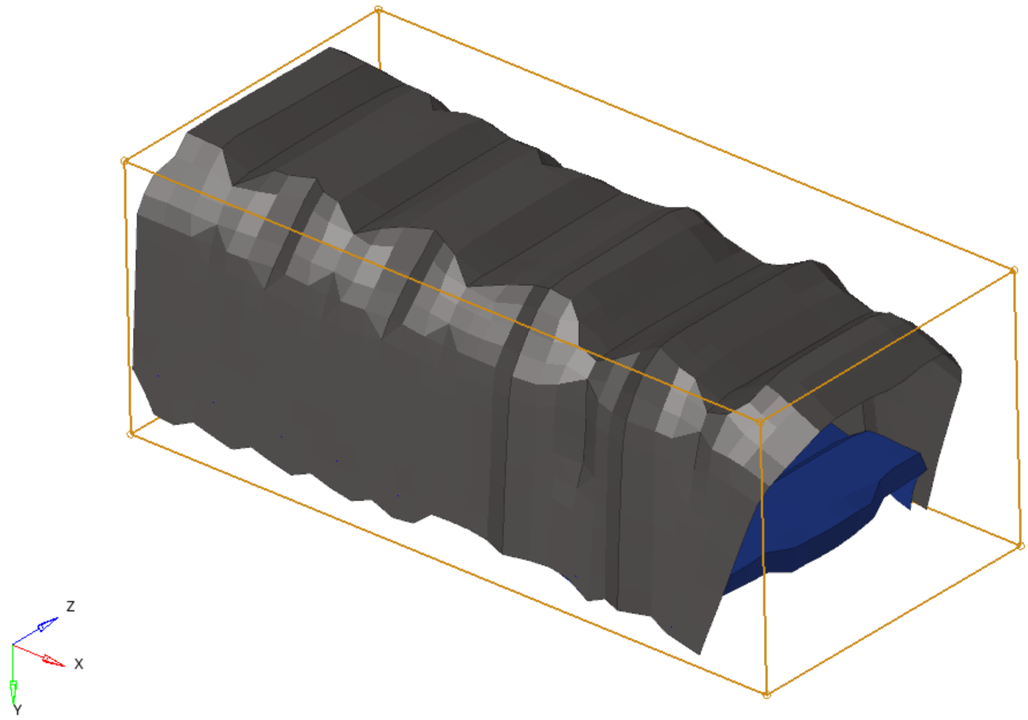


**FIGURE 4.3 – CRASH BOX'S MAXIMUM ENVELOPE**

# 4.2 Toyota Yaris' crash box performance

In the following, the results of the crash simulation on Toyota Yaris' component are shown, in order to consistently compare the mechanical performances of the lattice.

The structure is composed by an outer rail and a frame both made of steel, assembled together via spots welding. The geometry of the component is rather simple even though it includes some geometrical triggers along the longitudinal axis to induce the well-known folding mechanism. In this model, a PLANAR_FINITE_MOVING_DISPLAY rigid wall is defined which allows to specify the initial kinetic energy (Eq. 4.1), that the structure has to absorb by deformation. The structure is constrained at the other end by the application of SPC_SET boundary condition, which allows to constrain all the degrees of freedom except the rotation around the vertical axis. In order to calculate and compare the SEA of the Toyota Yaris' crash box, in the same way as done for the additive crash boxes, it is needed to evaluate at first the SEA as function of the deformed volume, then compute a mean value in a range in which it is quite constant and finally compute the SEA as function of the mass using the density of the material. So, concerning the evaluation of the SEA it is needed to evaluate an average area of the structure considering the mean value of three different cross sections. The resulting value is:

$$A_{avg} = 632.73\ mm^2$$

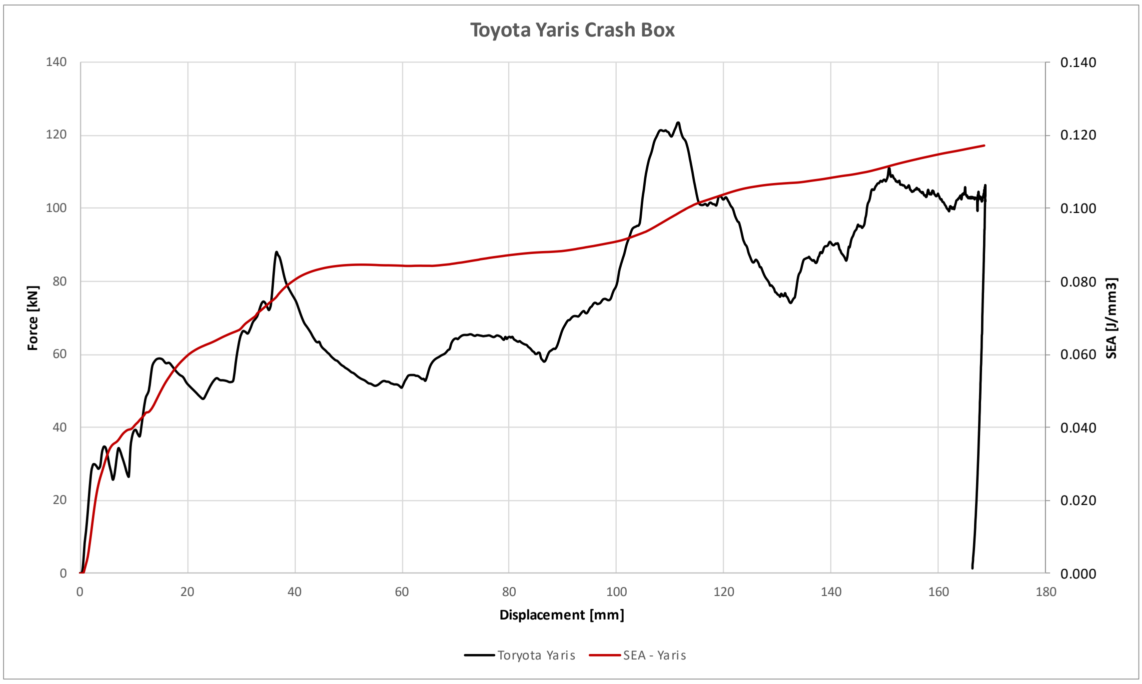


**FIGURE 4.4 - FORCE - DISPLACEMENT & SEA (TOYOTA YARIS)**

Figure 4.4 reports the force displacement trend of the Yaris crash box. In particular, it can be appreciated that several peaks and valleys are evident as result of the collapsing mechanism.

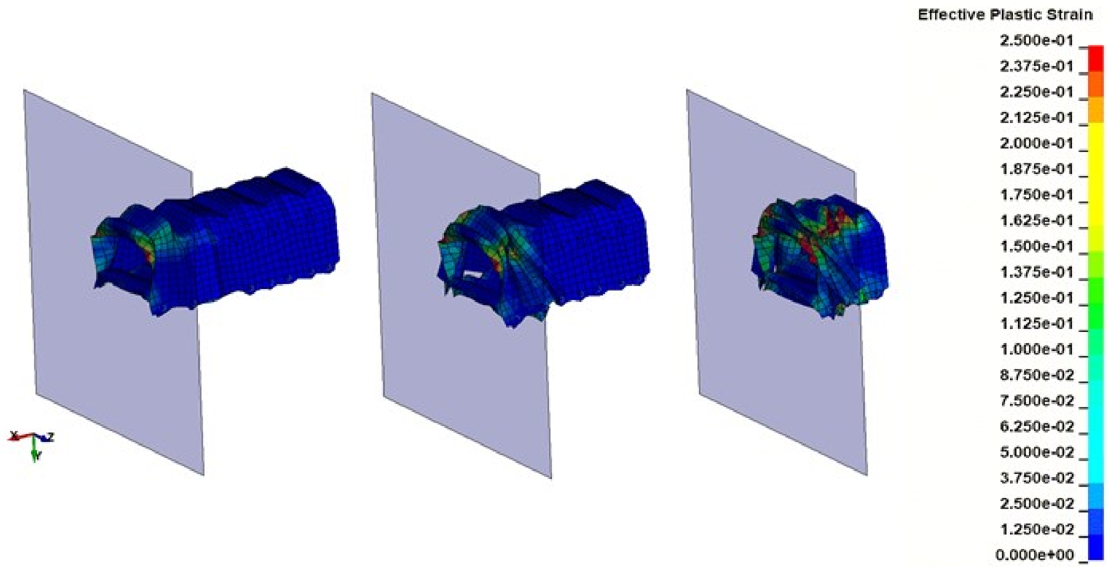


**FIGURE 4.5 - DEFORMATION OF TOYOTA YARIS' CRASH BOX**

In Figure 4.5, three frames of the deformation pattern are reported, where the effective plastic strain is contoured. It is clear that the geometrical triggers play a fundamental role to avoid buckling of the structure, while increasing the efficiency of the crash box. Each peak of the force displacement trend corresponds to the yielding of a specific area induced by the corresponding geometrical trigger. So, triggers are used to lower the peak force value and avoid in this way the buckling of the structure.

Another, important characteristic to be evaluated is the velocity diagram useful to compare the deceleration trends during the crash.

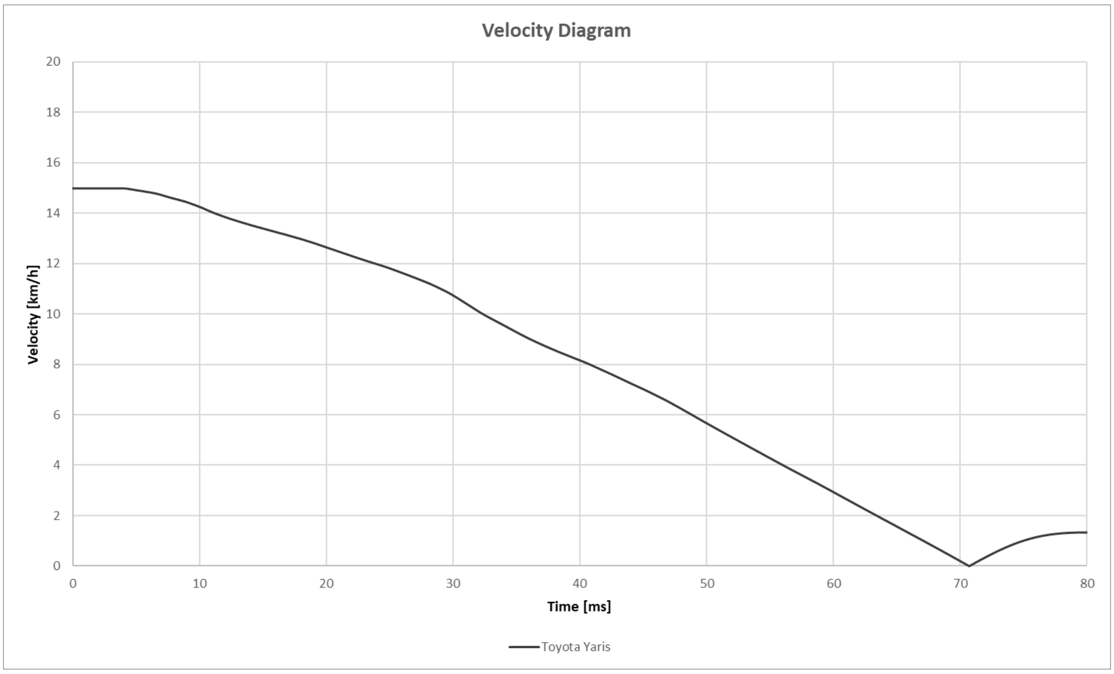


**FIGURE 4.6 - VELOCITY DIAGRAM (TOYOTA YARIS)**

To summarize the results, the main parameters about Toyota Yaris' crash box can be collected below:

| CRASH BOX | EA [J] | MASS [kg] | $SEA_{avg}$ [J/g] |
|---|---|---|---|
| **Toyota Yaris** | 10 301 | 1.054 | 12.32 |

**TABLE 4.1 - TOYOTA YARIS' CRASH BOX PERFORMANCE**

The SEA is here reported in terms of absorbed energy per unit of mass. In contrast to the definition considered in Chapter 3, the parameter as function of the structural mass is here preferred as it allows to consistently compare different structures made of different materials. Therefore, to compare efficiently the different structures, at first the average absorbed energy per unit of compressed volume is computed, then through the density it is possible to evaluate the parameter as function of the structural mass.

# 4.3 AM crash box version 1

The first concept of AM crash box simply consists of a repetition of the 12 FFP1 cell. The selected structure cell_12_FFP1 is thus used to fulfil the entire volume at disposal. This allow to investigate if the SEA and collapsing mechanism shown in the experimental tests are still valid at the macroscale of the component. The dimensions are limited in order to fulfil both manufacturing and envelope constraints.

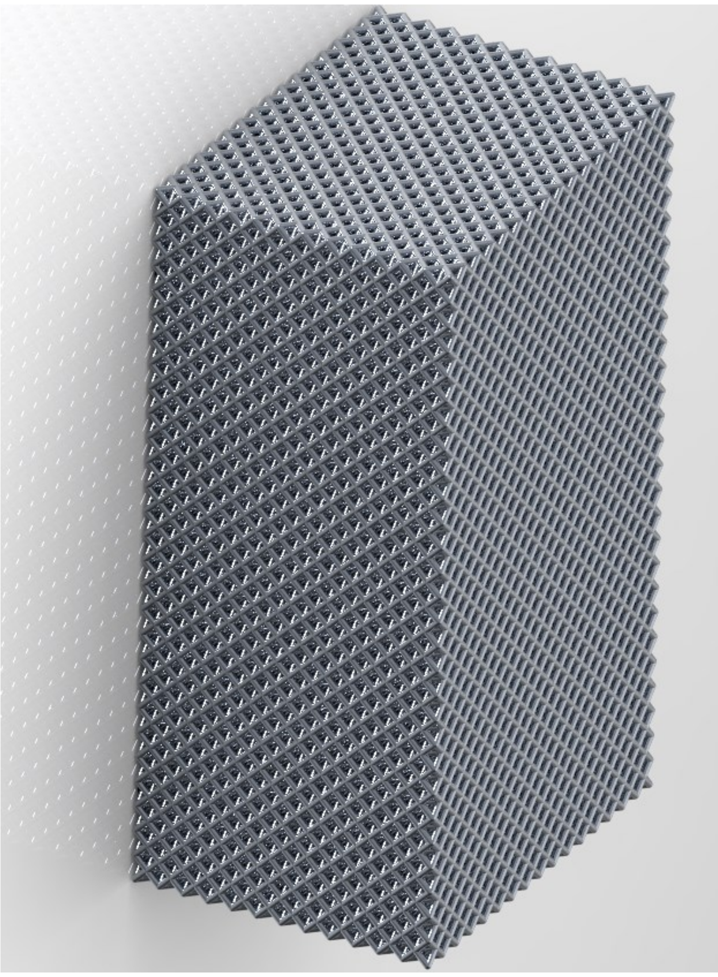

**FIGURE 4.7 - AM CRASH BOX VERSION 1**

The FEM model of this first version of the crash box includes at the base a rigid wall as a constrain. However, in the following will be understood that the application of SPC_SET as boundary constrain of the structure is more efficient from a computational point of view.

The results of the crash simulation are reported in Figure 4.8, where the stress contour at different crash instants is shown. It is possible to notice the same collapsing behaviour of experimental tests. The beams enter in the plastic field immediately after the beginning of the impact and the structure absorb the energy with a gradual compression.

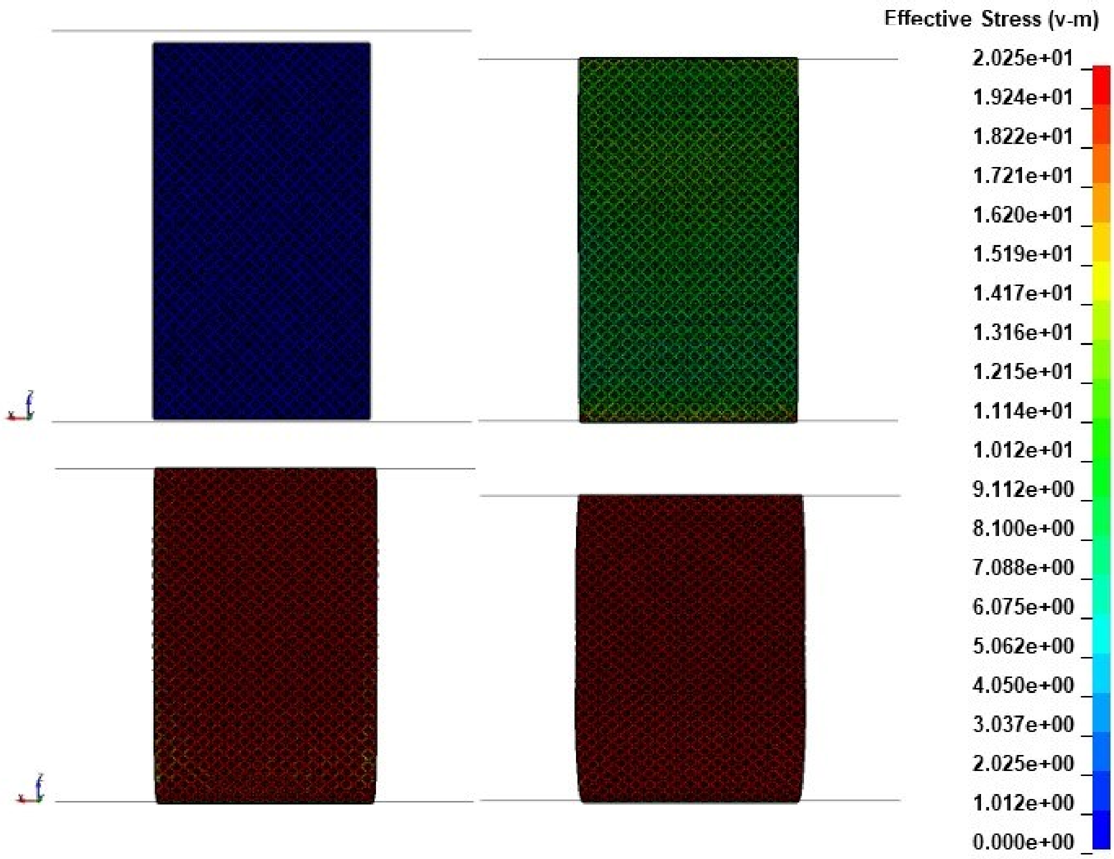


**FIGURE 4.8 – VON MISES STRESS AM CRASH BOX VERSION 1**

Figure 4.8 above show the stress pattern in the first instant of the crash, the iso-value shows a maximum value of 20.25 MPa, i.e. the yielding limit of material. However, once the structure has totally yielded, a global instability occurs as shown in Figure 4.9.

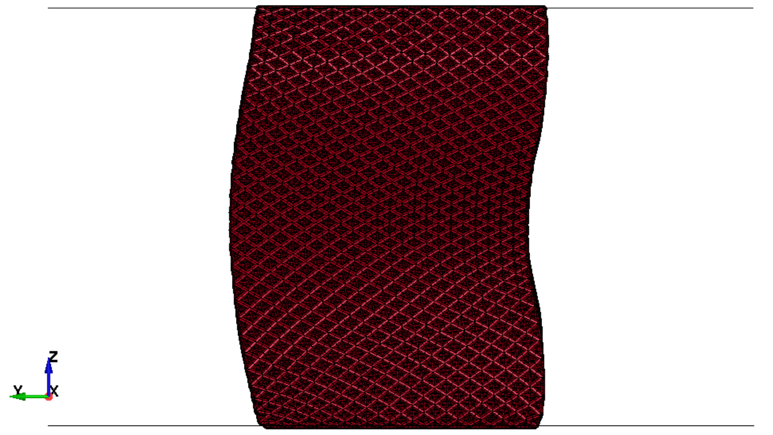


**FIGURE 4.9 – GLOBAL INSTABILITY OF AM CRASH BOX VERSION 1**

Probably, by increasing the number of layers, the equivalent length reaches a value that lower the critical load which is then encountered during the crushing phenomenon. To establish effectively if this kind of deformation is due to instability phenomena, a buckling analysis is performed. This kind of analysis is performed with Hypermesh (OptiStruct), and it determine the critical load in the following way:

$$[K - \lambda K_G]x = 0 \tag{4.3}$$

$$P_{cr} = \lambda_{cr} P_{ref} \tag{4.4}$$

The RWALL is substituted with a rigid element RBE2 in order to apply a reference load of 1 N. In this way, the solver will perform a simple linear static analysis to build the global stiffness matrix of the structure and then use them to evaluate the l factor. Choosing the reference load equal to 1 N means that in the post-processing of the analysis the value shown by the solver is directly the critical load. It must be taken into consideration that a slightly difference between the critical load evaluated with this procedure and the load value evaluated with crash simulation is expected, mainly due to the non-linearities introduced with the nonlinear analysis.

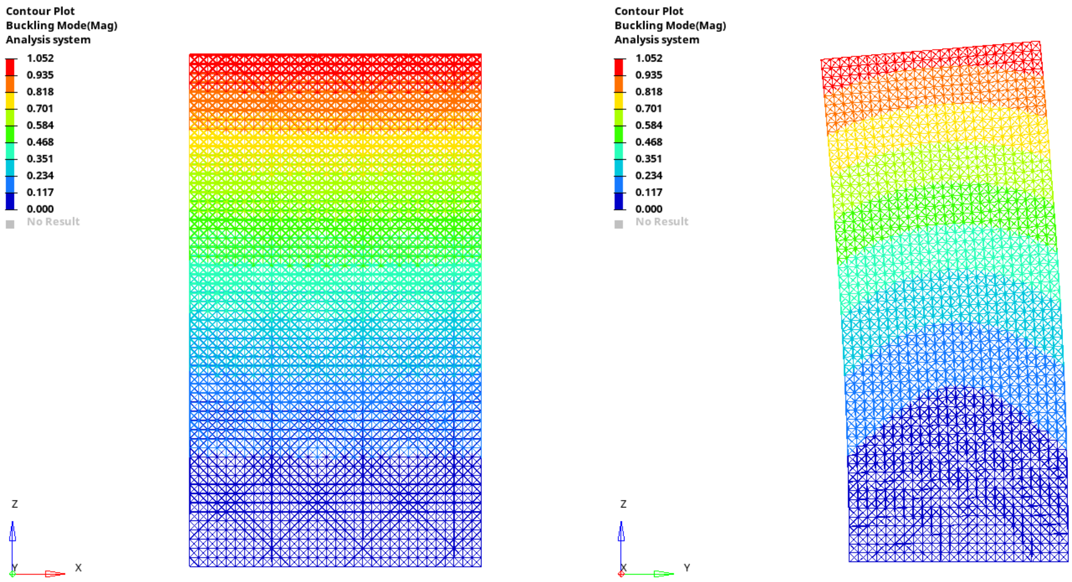


**FIGURE 4.10 - BUCKLING ANALYSIS OF AM CRASH BOX VERSION 1**

As represented in the Figure 4.10 above, it is clear that the deformation notice in the crash can be assessed to global instability of the structure, because the buckling mode is constrained by the presence of the RWALL results in the deformation represented in Figure 4.9. The critical value measured with buckling analysis is 117.26 kN. This load is surely exceeded by the structure because at the time instant represented before the load is about 130 kN . Besides, the buckling of the structure happened when the all the lattice beams overcome yielding, so the effective length is reduced with respect to the undeformed one. This is a possible reason of the discrepancy between the critical load evaluated with the buckling analysis and the effective one.

Recalling the general equation of global instability:

$$P_{cr} = \pi^2 \frac{E\,J}{L^2} \tag{4.5}$$

It is possible to overcome the global instability of the structure in the following way:

- Increasing the moment of inertia J
- Decreasing the effective length L

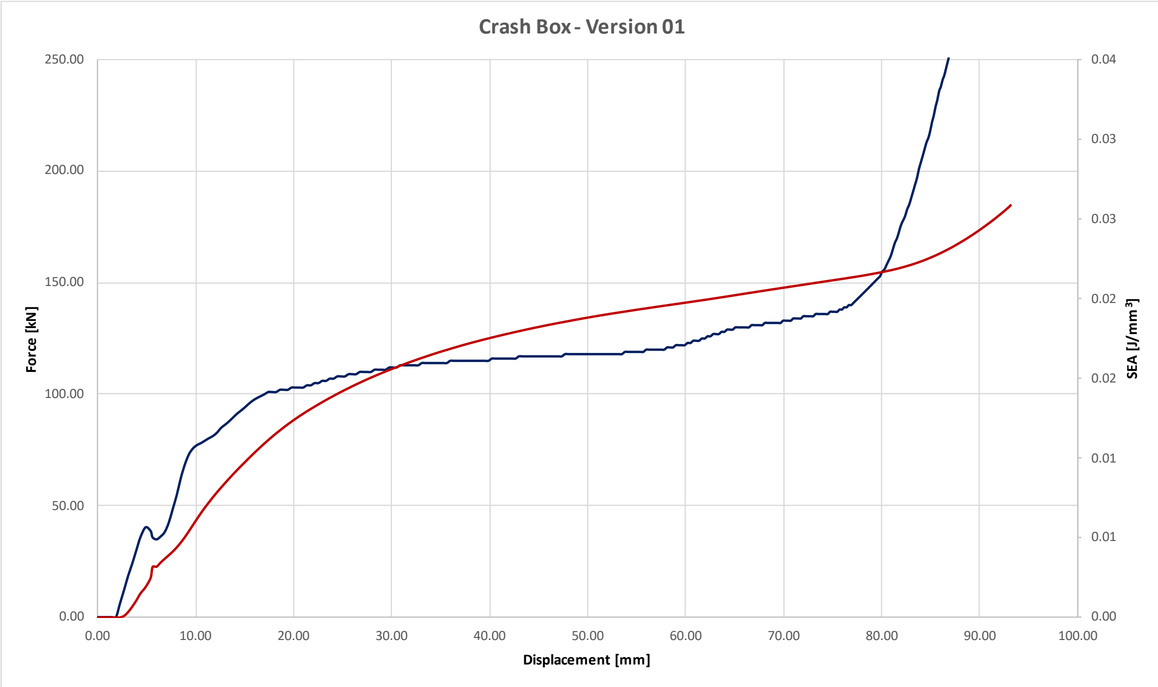


**FIGURE 4.11 - FORCE - DISPLACEMENT & SEA (AM CRASH BOX VERSION 1)**

The results shown in Figure 4.11 underline clearly the unchanged performances of the structure at macroscopic level. Global instability can be observed only analysing the deformed shape during the impact. However, this phenomenon has to be avoided in this kind of component, so in the following versions an increase of efficiency is expected.

| CRASH BOX | EA [J] | MASS [kg] | $SEA_{avg}$ [J/g] |
|---|---|---|---|
| **AM Crash Box Version 1** | 11 798.54 | 1.126 | 16.69 |

**TABLE 4.2 - AM CRASH BOX VERSION 1 PERFORMANCE**

This first version shows immediately that the efficiency of the crash box increase using this lattice structure (+35.5%). Energy absorption capacity is sufficient, the mass shows an increase of + 6.8% instead. In the following versions the main goals will be the decrease of the overall mass of the component, while maintaining unchanged the efficiency, and a stable collapsing mode.

## 4.4 AM crash box version 2

In order to avoid global instability, it is chosen to increase the average cross section area of the crash box using a 4x4 repetition instead of 3x4 of the version 1. This modification increases the moment of inertia J and so also the critical load. Besides, analysing in further details the previous configuration, it could be noticed that half of the structure does not contribute directly to the energy absorption, because the rebound phase starts after approximately 90 mm of displacement. Decreasing the height of the structure up to 108.3 mm (4 layers) contribute to the increase of the critical load, because the effective length of the structure is lower.

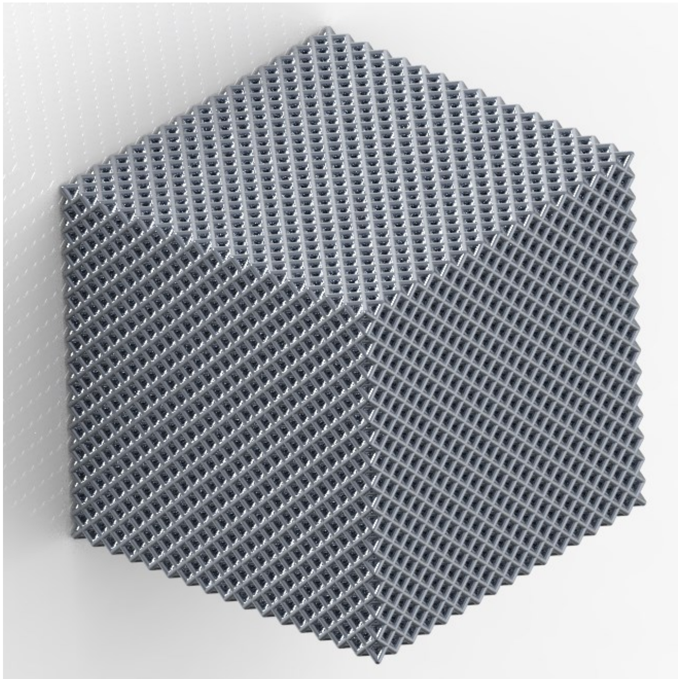

**FIGURE 4.12 - AM CRASH BOX VERSION 2**

This modification is also useful to decrease the mass. However, as stated in the previous chapter about factorial plan analysis, absorbing the energy in a lower volume leads to a steep deceleration of the impact. Therefore, when, performing the crash simulation, the deceleration will be carefully taken into consideration.

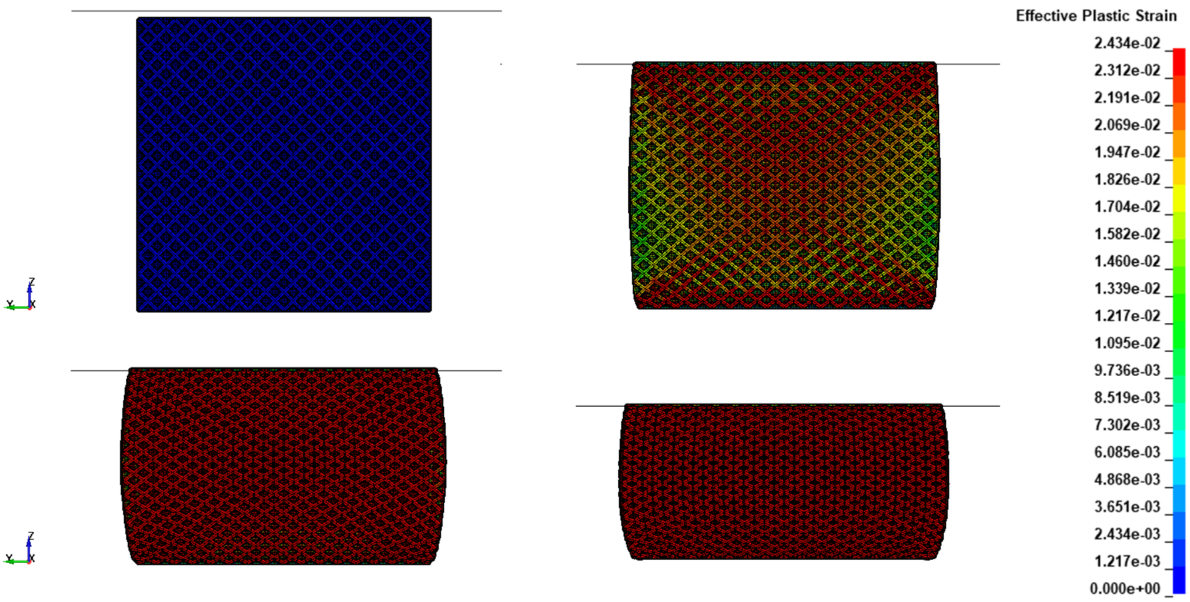


**FIGURE 4.13 - PLASTIC STRAIN OF AM CRASH BOX VERSION 2**

The analysis of the evolution of the plastic field during the impact does not lead to new details. Always, this collapsing mode is very similar to foam and the force versus displacement chart underlines an efficient trend, because the whole structure reaches the yielding globally avoiding peaks and valleys, exploiting a quite constant value of the force that leads to an increase of the absorbed energy (Figure 4.14).


**FIGURE 4.14 - FORCE - DISPLACEMENT & SEA (AM CRASH BOX VERSION 2)**

The mean load is increased and also from the deformation it is clear that in this case instability is avoided. What is important to notice is that the overall energy absorbed up to densification is about 11 792 J and for version 2 the total displacement is about 40 mm. So, the amount of energy is more or less the same of version 1, but the total displacement up to densification is decreased of about - 47%. The very steep deceleration obtained through this structure can be also appreciated in comparison with the velocity diagram of the Toyota Yaris component. The velocity diagrams are particularly compared in Figure 4.15.

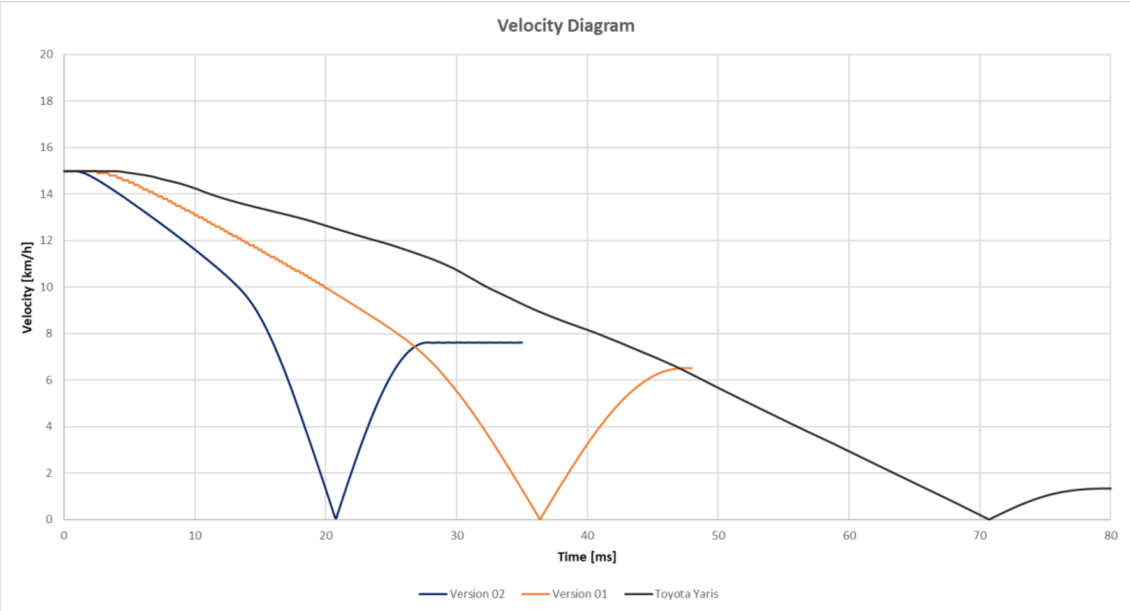


**FIGURE 4.15 - VELOCITY DIAGRAM COMPARISON (VERSION 2)**

Naturally, performing the integral it is expected that the peak of acceleration for version 2 will be higher with respect to the others. Without a full-scale approach, it is very difficult to know if this amount of acceleration is sustainable or not, so it is needed to improve the deceleration characteristic of AM crash box in order to get closer to the reference of Toyota Yaris. For this aim, as already stated as conclusion of the factorial plan analysis, a suitable solution is to increase the longitudinal dimension of the crashbox and adopting a variable diameter of the beams of the lattice, in order to obtain a gradual reaction to the crash. It is expected to lose some points about efficiency, but great advantages in terms of deceleration could be reached.

| CRASH BOX | EA [J] | MASS [kg] | $SEA_{avg}$ [J/g] |
|---|---|---|---|
| **AM Crash Box Version 2** | 11 792 | 0.859 | 16.72 |

**TABLE 4.3 - AM CRASH BOX VERSION 2 PERFORMANCE**

Another disadvantage of this version regards the dimension constraint set at the beginning of our design. In fact, in order to consider a realistic case, the main dimensions of the crash box are fixed by the reference volume of Toyota Yaris' component.

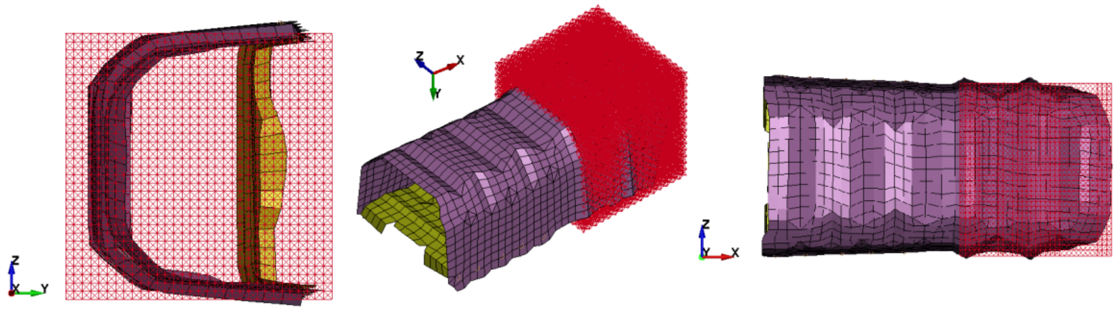

**FIGURE 4.16 - COMPARISON OF DIMENSION OF CRASH BOX VERSION 2**

The vertical dimension of version 2 is within the constrained limit, the longitudinal dimension is decreased to a third more or less, the lateral direction (Y) exceeds the limits instead. So, from a packaging point of view also this dimension must be fixed: the increase in dimension is about 51 mm which corresponds to the size of 2 cell units.

Furthermore, the following versions will introduce beams with variable diameter along the structure and the lateral dimension of the structure will be reduced within the limits.

# 4.5 AM crash box version 3 & 4

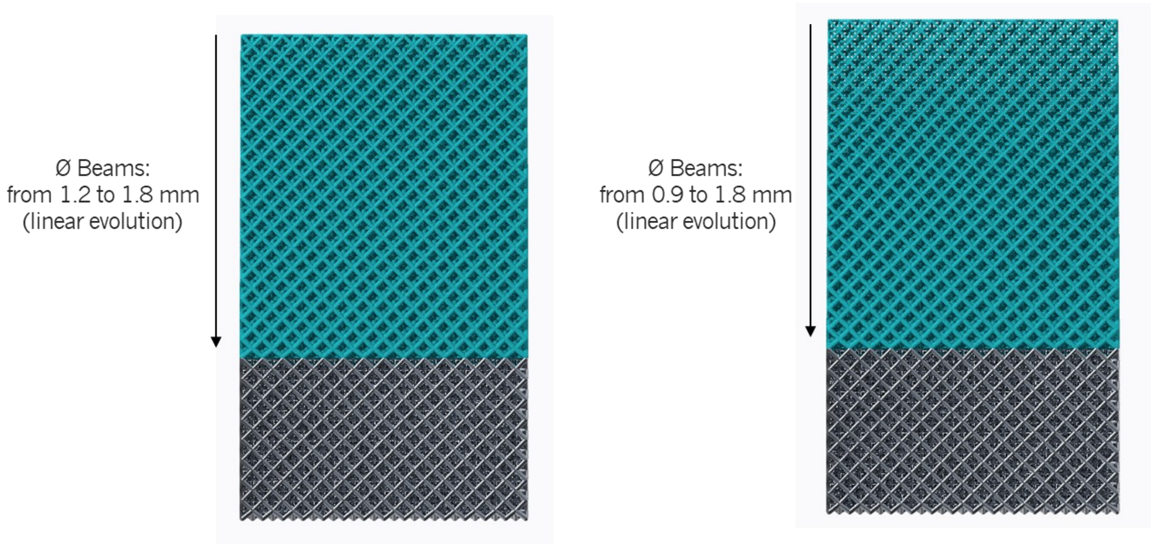


**FIGURE 4.17 - AM CRASH BOXES VERSION 3 & 4**

The new versions of the AM crash box are represented in Figure 4.17. The layout is very simple: the grey zone has a structure similar to previous versions with the diameter of the beams equal to 1.8 mm to guarantee that the average load will be in the order of magnitude of versions before. Then, there is the introduction of the transition zone in which the diameter of the beams is defined with a linear evolution ranging from a minimum of 1.2 or 0.9 mm to a maximum equal to 1.8 mm. This part of the crash box is used in order to improve the deceleration characteristics. Indeed, as underlined in the analysis of the factorial plans, the only factor of influence in the repetition of the structure in the space is related to the diameter of the beams. Furthermore, including a progressive definition of the diameters it is possible to obtain a performance very similar to the one exploited by tapered crash boxes, i.e. a progressive reaction to the crash. In this way, it is possible to increase the volume of the component to absorb the same amount of energy through a larger displacement. The global instability in this case is avoided because every longitudinal step corresponds to a different critical load that will be for sure higher with respect to the average load in that instant. Besides, also the lateral dimension of the crash box is decreased of 51 mm to be in the reference limits.

The post processing of the results requires a step definition of the average area in order to consider in the evaluation of the SEA, instant by instant, the corrected area.

| Version 3 | Z coordinate [mm] | Diameter null beam [mm] | Effective Diameter [mm] | Area [$mm^2$] |
|---|---|---|---|---|
| Step 25 | 0.0 | 1.20 | 1.11 | 181.20 |
| Step 26 | 3.2 | 1.22 | 1.13 | 186.91 |
| Step 27 | 6.4 | 1.24 | 1.14 | 192.71 |
| Step 28 | 9.6 | 1.26 | 1.16 | 198.59 |
| Step 29 | 12.8 | 1.28 | 1.18 | 204.56 |
| Step 30 | 15.9 | 1.29 | 1.20 | 210.62 |
| Step 31 | 19.1 | 1.31 | 1.21 | 216.77 |
| Step 32 | 22.3 | 1.33 | 1.23 | 223.01 |
| Step 1 | 25.5 | 1.35 | 1.25 | 229.34 |
| Step 2 | 28.7 | 1.37 | 1.27 | 235.75 |
| Step 3 | 31.9 | 1.39 | 1.28 | 242.25 |
| Step 4 | 35.1 | 1.41 | 1.30 | 248.85 |
| Step 5 | 38.3 | 1.43 | 1.32 | 255.53 |
| Step 6 | 41.4 | 1.44 | 1.34 | 262.29 |
| Step 7 | 44.6 | 1.46 | 1.35 | 269.15 |
| Step 8 | 47.8 | 1.48 | 1.37 | 276.10 |
| Step 9 | 51.0 | 1.50 | 1.39 | 283.13 |
| Step 10 | 54.2 | 1.52 | 1.40 | 290.25 |
| Step 11 | 57.4 | 1.54 | 1.42 | 297.47 |
| Step 12 | 60.6 | 1.56 | 1.44 | 304.76 |
| Step 13 | 63.8 | 1.58 | 1.46 | 312.15 |
| Step 14 | 66.9 | 1.59 | 1.47 | 319.63 |
| Step 15 | 70.1 | 1.61 | 1.49 | 327.19 |
| Step 16 | 73.3 | 1.63 | 1.51 | 334.85 |
| Step 17 | 76.5 | 1.65 | 1.53 | 342.59 |
| Step 18 | 79.7 | 1.67 | 1.54 | 350.42 |
| Step 19 | 82.9 | 1.69 | 1.56 | 358.34 |
| Step 20 | 86.1 | 1.71 | 1.58 | 366.35 |
| Step 21 | 89.3 | 1.73 | 1.60 | 374.44 |
| Step 22 | 92.4 | 1.74 | 1.61 | 382.63 |
| Step 23 | 95.6 | 1.76 | 1.63 | 390.90 |
| Step 24 | 98.8 | 1.78 | 1.65 | 399.26 |

**TABLE 4.4 - LINEAR DEFINITION OF VARIABLE BEAMS (VERSION 3)**

| Version 4 | Z coordinate [mm] | Diameter null beam [mm] | Effective Diameter [mm] | Area [$mm^2$] |
|---|---|---|---|---|
| Step 25 | 0.00 | 0.90 | 0.83 | 101.93 |
| Step 26 | 3.19 | 0.93 | 0.86 | 108.40 |
| Step 27 | 6.38 | 0.96 | 0.88 | 115.07 |
| Step 28 | 9.56 | 0.98 | 0.91 | 121.93 |
| Step 29 | 12.75 | 1.01 | 0.94 | 129.00 |
| Step 30 | 15.94 | 1.04 | 0.96 | 136.27 |
| Step 31 | 19.13 | 1.07 | 0.99 | 143.73 |
| Step 32 | 22.31 | 1.10 | 1.01 | 151.40 |
| Step 1 | 25.50 | 1.13 | 1.04 | 159.26 |
| Step 2 | 28.69 | 1.15 | 1.07 | 167.32 |
| Step 3 | 31.88 | 1.18 | 1.09 | 175.59 |
| Step 4 | 35.06 | 1.21 | 1.12 | 184.05 |
| Step 5 | 38.25 | 1.24 | 1.14 | 192.71 |
| Step 6 | 41.44 | 1.27 | 1.17 | 201.57 |
| Step 7 | 44.63 | 1.29 | 1.20 | 210.62 |
| Step 8 | 47.81 | 1.32 | 1.22 | 219.88 |
| Step 9 | 51.00 | 1.35 | 1.25 | 229.34 |
| Step 10 | 54.19 | 1.38 | 1.27 | 238.99 |
| Step 11 | 57.38 | 1.41 | 1.30 | 248.85 |
| Step 12 | 60.56 | 1.43 | 1.33 | 258.90 |
| Step 13 | 63.75 | 1.46 | 1.35 | 269.15 |
| Step 14 | 66.94 | 1.49 | 1.38 | 279.60 |
| Step 15 | 70.13 | 1.52 | 1.40 | 290.25 |
| Step 16 | 73.31 | 1.55 | 1.43 | 301.10 |
| Step 17 | 76.50 | 1.58 | 1.46 | 312.15 |
| Step 18 | 79.69 | 1.60 | 1.48 | 323.40 |
| Step 19 | 82.88 | 1.63 | 1.51 | 334.85 |
| Step 20 | 86.06 | 1.66 | 1.53 | 346.49 |
| Step 21 | 89.25 | 1.69 | 1.56 | 358.34 |
| Step 22 | 92.44 | 1.72 | 1.59 | 370.38 |
| Step 23 | 95.63 | 1.74 | 1.61 | 382.63 |
| Step 24 | 98.81 | 1.77 | 1.64 | 395.07 |

**TABLE 4.5 - LINEAR DEFINITION OF VARIABLE BEAMS (VERSION 4)**

So, as a function of the Z local coordinate, it is possible to choose the correct average area corresponding a specific instant of the crash. The two columns related to the diameter are defined with the same linear function and correspond to the definition of the effective beams and null beams in the FEM model.

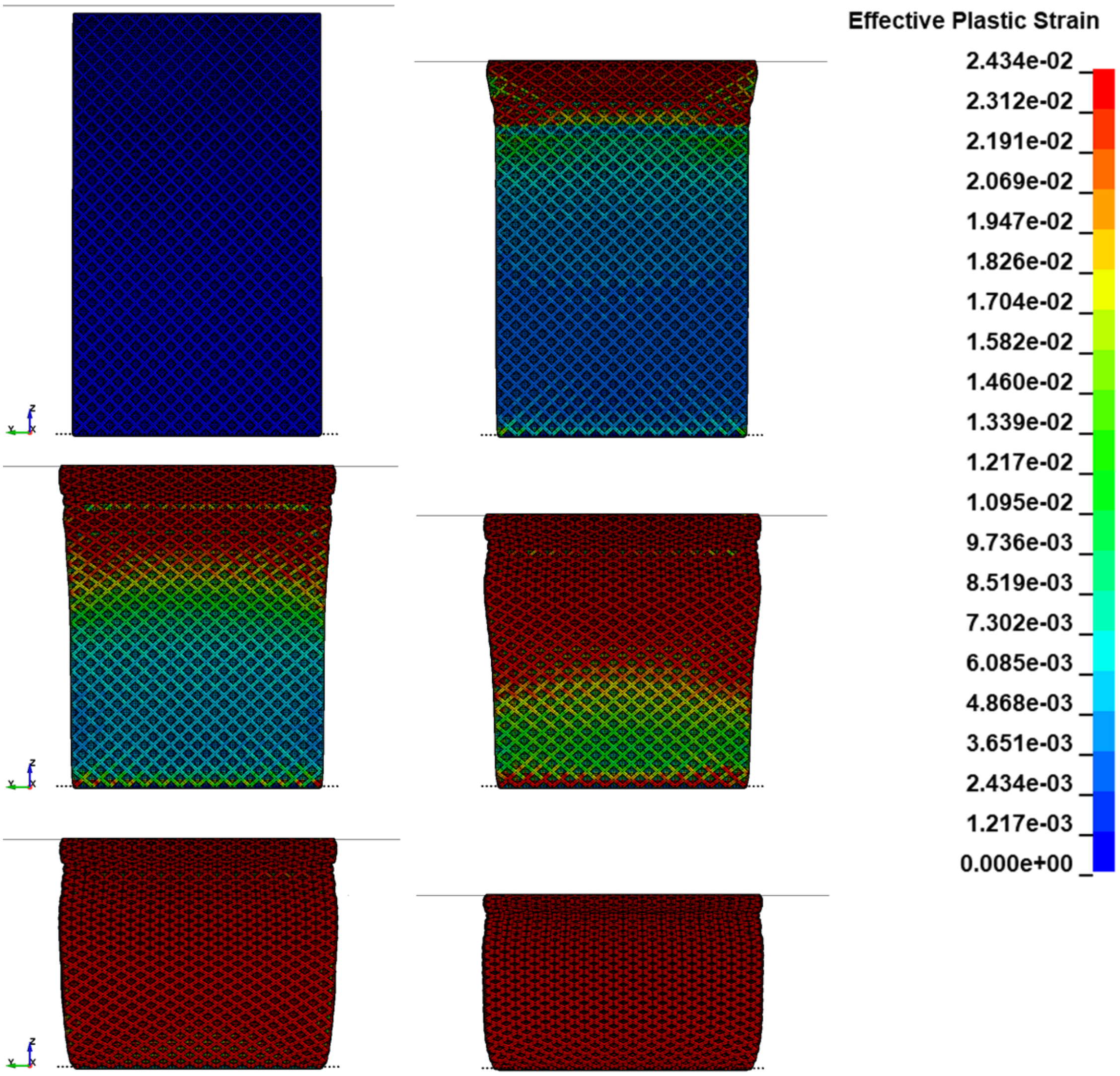


**FIGURE 4.18 - PLASTIC STRAIN OF AM CRASH BOX VERSION 3**

Starting from the analysis of version 3, it is possible to notice that the structure collapse within the first 55 mm of displacement with a shape like a cone. This fact underlines the progressive reaction to the crash sustained by the component. Also, it is important that all the structure immediately yields at the contact with the RWALL, but then collapses progressively. Global instability is avoided as expected.

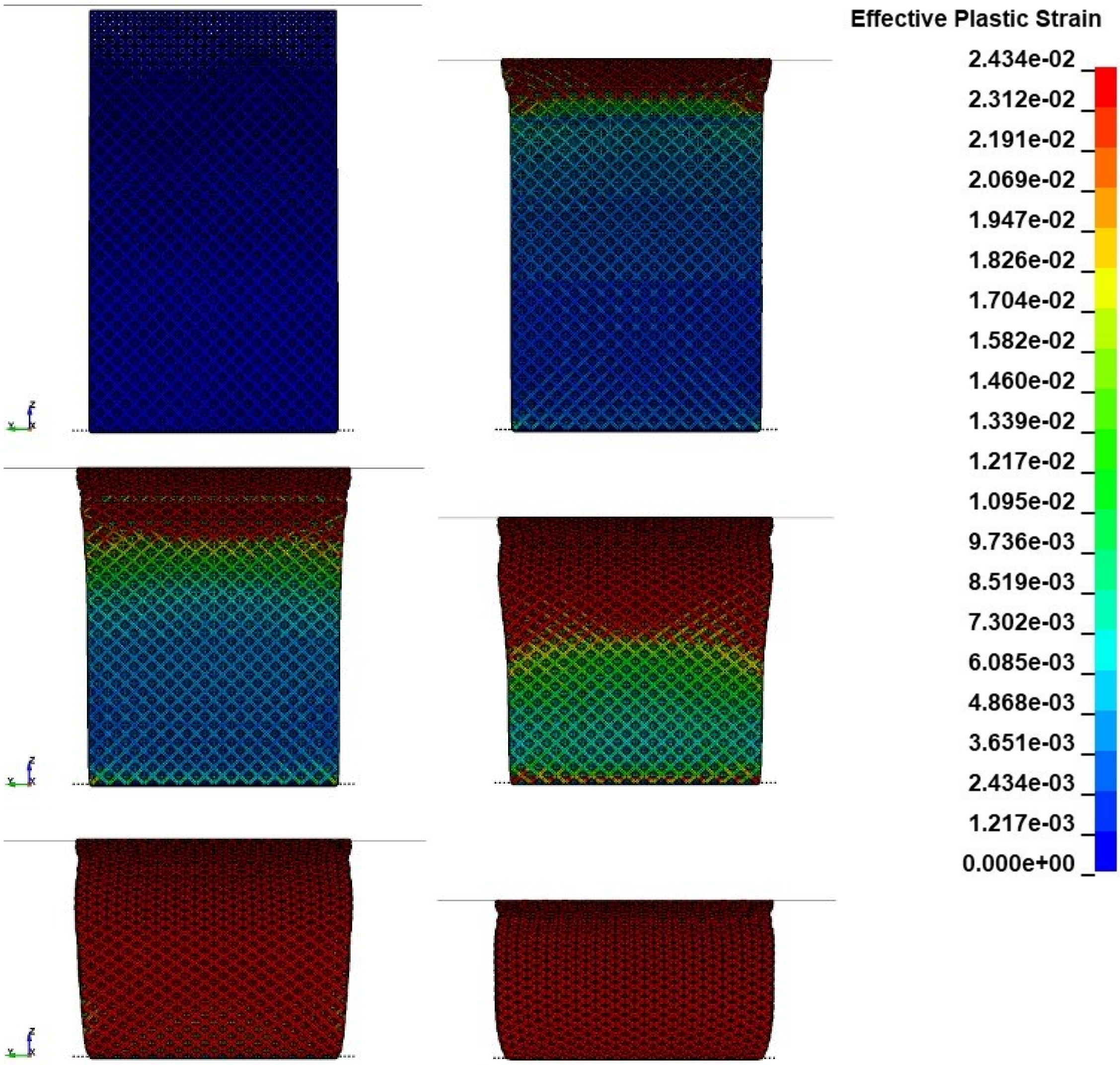


**FIGURE 4.19 - PLASTIC STRAIN OF AM CRASH BOX VERSION 4**

Figure 4.19 represents the plastic strain evolution of the version 4. There are not so evident differences with respect to version 3 except for the first phase in which the structure collapse more easily due to the reduced diameter of the beams. To define better the performances of these versions, it is convenient to compare the force-displacement curves with the reference of Toyota Yaris. Obviously, comparing the SEA function, the versions 3 and 4 will exploit a step definition as stated previously with the definition of linear evolution of the average area.

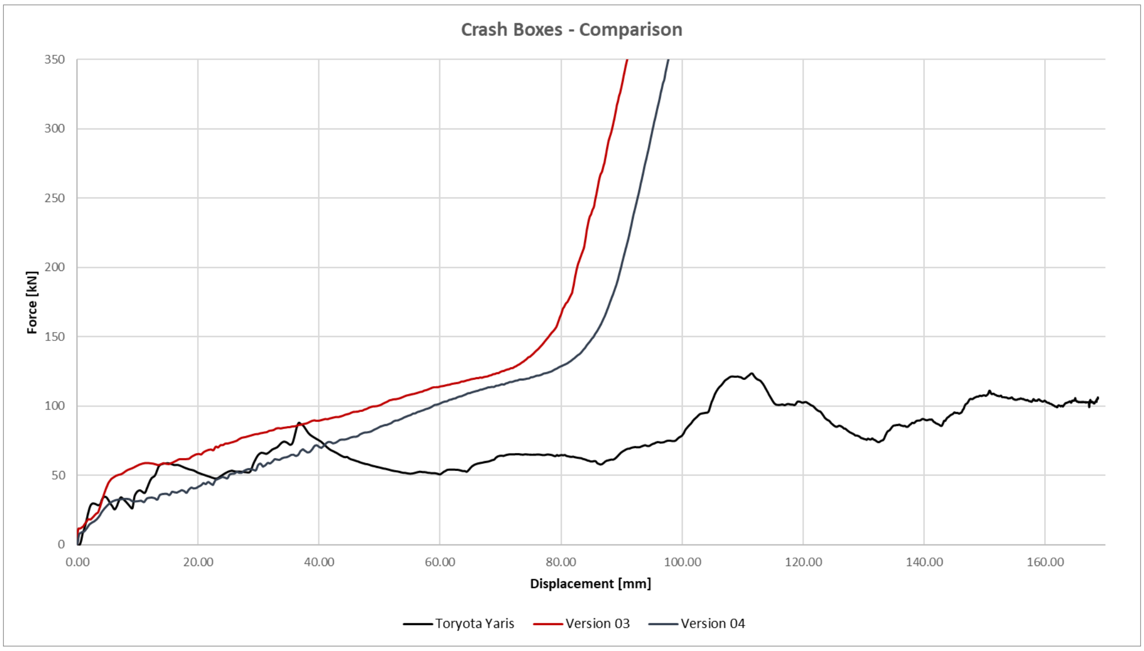


**FIGURE 4.20 - FORCE - DISPLACEMENT (AM CRASH BOXES VERSION 3 & 4)**

The force versus displacement chart underlines the evident difference between a folding and gradual compression collapsing mode. However, as it could be seen in the next graph, the adoption of carbon nylon lattice structure is convenient from a point of view of the masses and efficiency. The main disadvantage is always related to the deceleration, even if these versions underline a better behaviour from this point of view. Approaching about 80 mm of displacement, the lattice crash boxes enter into densification region. Therefore, the resulting force rise steeply increasing also the deceleration associated to. A further improvement, that can lead to benefits from this point of view, is related to the increase of the total length of the structure. Probably, the mechanical response will be smoother because the same amount of kinetic energy will be absorbed in a larger volume. Thereafter, the main difference between version 3 and 4 is the different linear definition of the variable regions, that will certainly highlight the best deceleration profile for version 4 and the highest efficiency for version 3.

It could be interesting focus the attention on the first 10 mm of the impact. It can be notice that the AM versions exploit a lower tangent with respect to Toyota Yaris, that can be convenient for VRU (Vulnerable Road Users) crashes. In fact, the lattice structures evidence a less stiff reaction to a very weak impact, that results for sure in a lower damage of the vulnerable users.

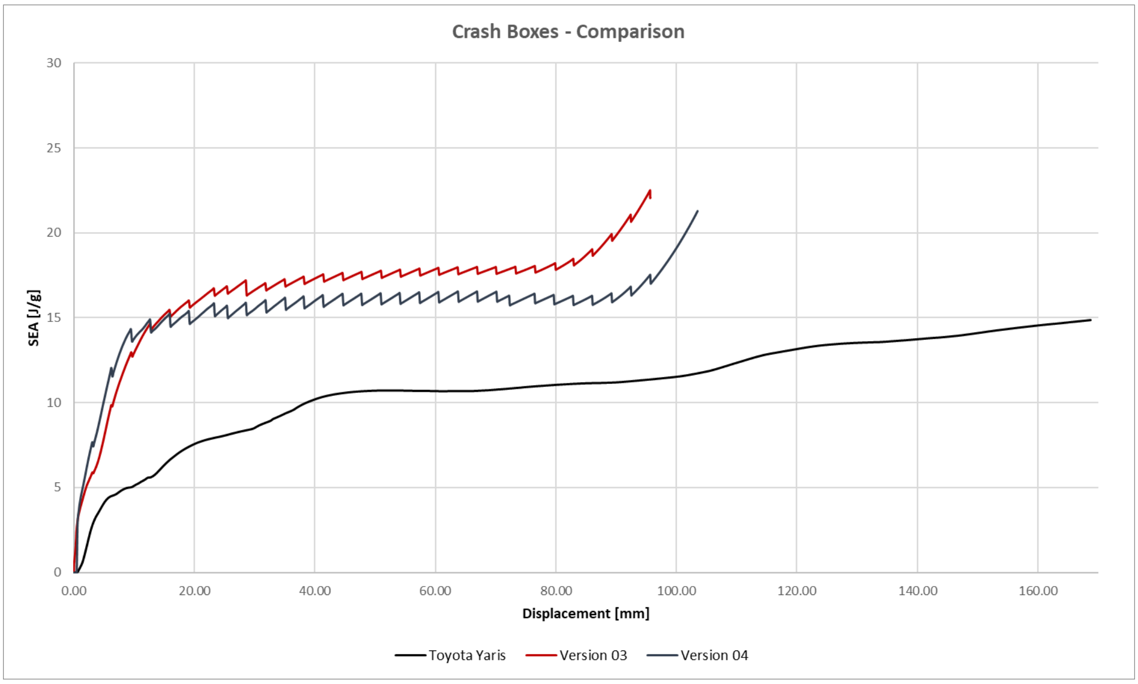


**FIGURE 4.21 - SEA (AM CRASH BOXES VERSION 3 & 4)**

In regard to the SEA, these AM versions underline a higher efficiency with respect to the standard configuration previously investigated. A decrease of the structural mass is obviously achieved. In the table below, the obtained results will be summarized.

| CRASH BOX | EA [J] | MASS [kg] | $SEA_{avg}$ [J/g] |
|---|---|---|---|
| **AM Crash Box Version 03** | 11 779 | 0.846 | 17.48 |

**TABLE 4.6 - AM CRASH BOX VERSION 3 PERFORMANCE**

| CRASH BOX | EA [J] | MASS [kg] | $SEA_{avg}$ [J/g] |
|---|---|---|---|
| **AM Crash Box Version 04** | 11 771 | 0.772 | 15.98 |

**TABLE 4.7 - AM CRASH BOX VERSION 4 PERFORMANCE**

These last versions represent two different suitable solutions. From one side, the version 3 exploits a higher efficiency, but the most advantageous solution is clearly the version 4 because shows a further decrease of the mass with respect to the reference.

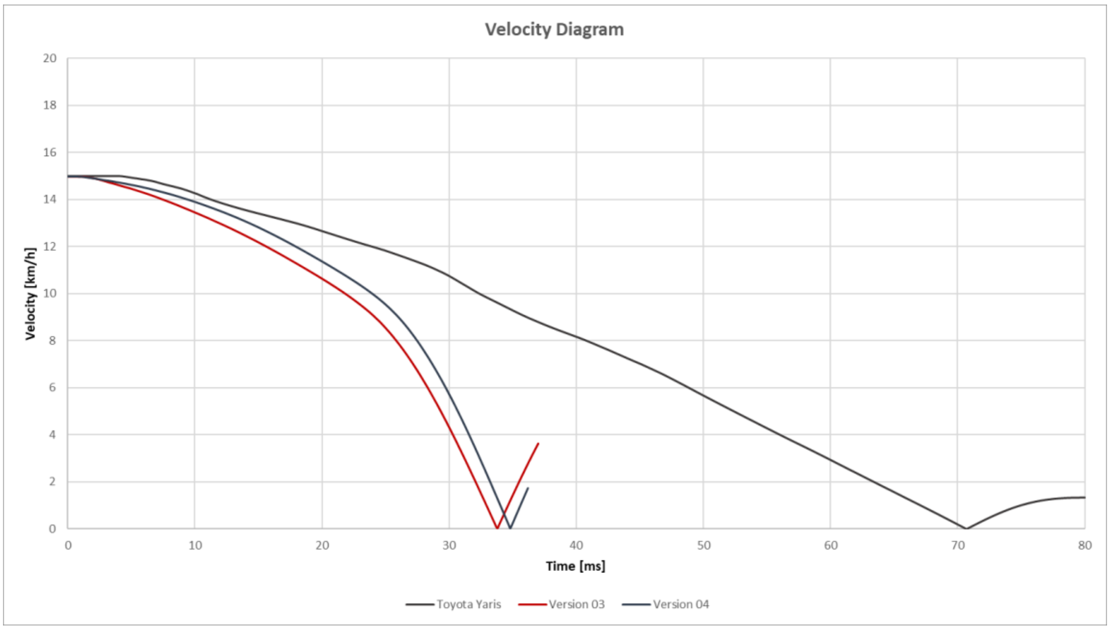


**FIGURE 4.22 - VELOCITY DIAGRAM (VERSION 03 & 04)**

Also, analysing the velocity diagram with a comparison with the reference of Toyota Yaris, it is possible to notice that up to 10 ms the performances are very closed to the reference. Then, from 10 to 20 ms, the deceleration of version 3 and 4 is increased a little bit, remaining anyway very near to the reference acceleration. After 20 ms there is a relevant increase in acceleration up to 25-27 ms when densification occurs.

So, both the versions exploit a deceleration characteristic very closed to the reference up to 75% of its total deformation. It could be possible the introduction of additional layers, but effectively the reference velocity trend of Toyota Yaris would be difficult to reach because of the different collapsing mechanism. Also, from a manufacturing point of view, with version 4 the main dimension of the crash box is very closed to the limit dimension of the 3D printing machine used.

# Conclusion

The experimental analysis carried out in this thesis underlines some advice for the design of AM crash boxes. Particularly, the main influential parameters, about the energy absorption capacity of lattice structure, have been evaluated, through an experimental approach, in order to increase effectively the SEA of AM crash boxes.

These key aspects, about the design of lattice structures, have been used to design a crash box and compare them with the Toyota Yaris' crash box. The obtained results with the designed AM crash box Version 04 are satisfactory, and the improvements are here reported:

- Structural mass of the crash box decreased of 26.7% (772 g)
- $SEA_{avg}$ improved up to 15.98 J/g (+29.7%)
- Deceleration quite similar up to densification

Besides, a FEA model has been at first experimentally correlated, to have a reliable tool, at disposal, to simulate the structural response of the different versions of the crash box.

Further development of this work can be carried out, starting from an optimization process in order to find out which is the main factor of influence about the definition of a structure with variable beams along its axis. Some simulations have been performed about this topic and positive results are expected.

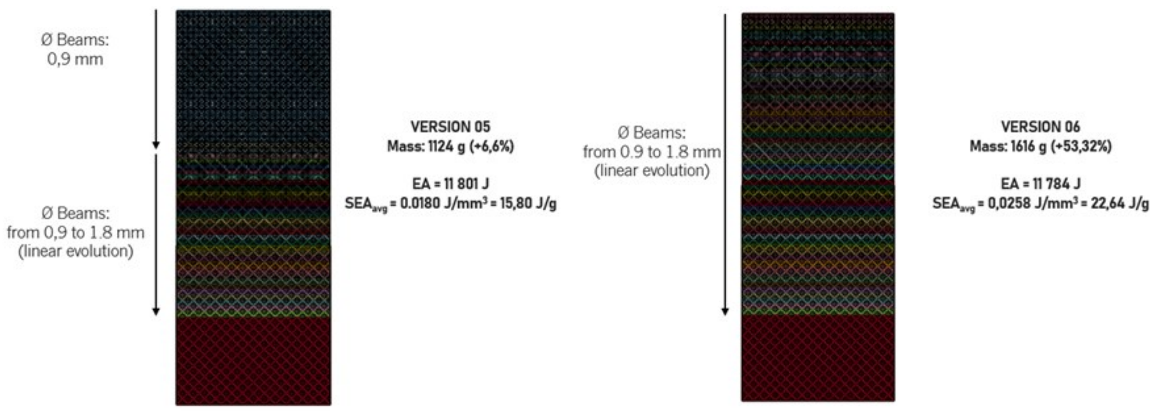


**FIGURE 5.1 - AM CRASH BOXES VERSIONS 05 AND 06**

Figure 5.1 shows the morphology of the abovementioned structures. In these cases, the variable region of the beams is extended up to about 230 mm in order to improve the deceleration after the impact. The results in these terms show positive advantages, but in terms of structural mass show an increase at least of 6.6%. For these reasons further optimization of a completely variable geometry of the AM crash box could lead to performances improvements.

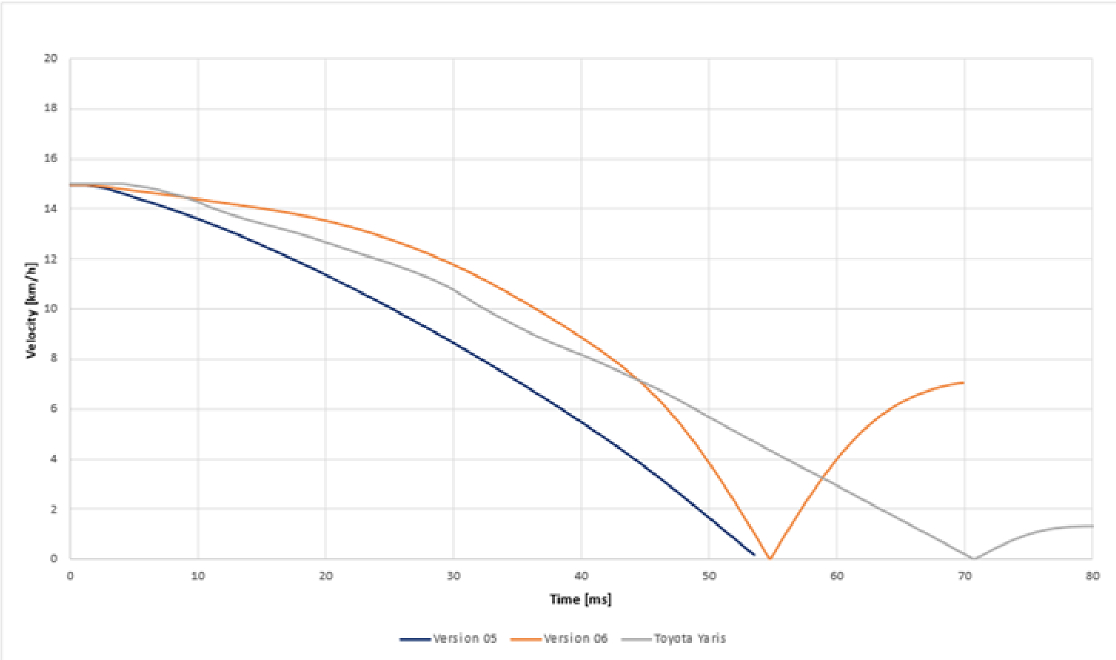


**FIGURE 5.2 - VERSION 05 AND 06 OF AM CRASH BOX**

The Figure 5.1 reports the velocity diagram of two additional versions of the AM crash box. Particularly, the Version 05 shows a SEA of 15.80 J/g (+28.25%) and, especially, a velocity gradient very similar to the one of Toyota Yaris structure. The benefits, in terms of deceleration, are related to the densification phase. Version 05 does not show a densification phase up to the end of the crush, exploiting a velocity diagram very similar to Toyota Yaris. Instead, Version 06 shows a much better behaviour with respect to the reference up to densification, in terms of deceleration.

Therefore, further studies about variable beam structures lead to considerable improvements , increasing the performances of AM crash boxes.

# REFERENCES

[1] Flaviana Calignano, M. L. (4 September 2020). Investigation of the Mechanical Properties of a Carbon Fibre-Reinforced Nylon Filament for 3D Printing. Machines.

[2] Mariano, D. R. (2020 - 2021). M.Sc. Thesis: Provini in struttura lattice realizzati mediante fabbricazione additiva: Simulazione di prove statiche e di impatto e validazione sperimentale.

[3] Emily Owen, O. (Jan 2020). LS-DYNA Introduction to contacts.

[4] LSTC. (2019). LS-DYNA Theory Manual.

[5] Recep M Gorguluarslan, Gungor, U., Yıl, S., & Erem, E. (2019). Lattice-Based Crash Box Design by Discrete Topology Optimization For 3D. ResearchGate.

[6] Xian Wu, Shuxian Zhang, & Jianwang Shao. (2018). Studies on Impact Performance of Gradient Lattice Structure Applied to Crash Box. SAE.

[7] Sing Ying Choy, Chen-Nan Sun, Kah Fai Leong, & Jun Wei. (2017). Compressive properties of Ti-6Al-4V lattice structures fabricated by selective laser melting: Design, orientation and density. Elsevier.

[8] L. Boniotti, S. Beretta, S. Folletti, & L. Patriarca. (2017). Strain concentration in BCC micro lattices obtained by AM. Elsevier.

[9] Erhan Cetin, & Cengiz Baykasoğlu. (n.d.). Energy absorption of thin-walled tubes enhanced by lattice structures. Elsevier.

[10] N.S.B. Yusof, S.M. Sapuan, M.T.H. Sultan, M. Jawaid, & M.A. Maleque. (2017). Design and materials development of automotive crash box: a review. Elsevier España.

[10] N.S.B. Yusof, S.M. Sapuan, M.T.H. Sultan, M. Jawaid, & M.A. Maleque. (2017). Design and materials development of automotive crash box: a review. Elsevier España.

[11] Luca Benedetto. (2020 - 2021). M.Sc. Thesis: Studio del comportamento ad impatto di una crash box innovativa in composito con struttura Origami.

[12] European Aluminium Association. (2013). Applications - Car Body - Crash Management System. The Aluminium Automotive Manual.

[13] Mario Boreanaz. (n.d.). M.Sc. Thesis: Development of crash box for automotive application.

[14] Julian Happian-Smith. (2002). An Introduction to Modern Vehicle Design. Reed Educational and Professional Publishing Ltd.

[15] Lorenzo Morello, Lorenzo Rosti Rossini, Giuseppe Pia, & Andrea Tonoli. (n.d.). The Automotive Body Volume I: Components Design. Springer.

[16] Research Council for Automotive Repairs. (2011). RCAR Low-speed structural crash test protocol.

[17] National Crash Analysis Center at The George Washington University (2019). FE model of 2010 Toyota Yaris